Duan F, Hu Z, Wang J.

Investigation of the VIMs of a spar-type FOWT using a model test method.

***Journal of Renewable and Sustainable Energy* 2016, 8(6), 063301.**

Investigation of the VIMs of a spar-type FOWT using a model test method

Fei Duan[1], Zhiqiang Hu[1,2]*, Jin Wang[1,3]

[1] State Key Laboratory of Ocean Engineering, Shanghai Jiao Tong University, 800 Dongchuan Road, 200240, Shanghai, China

[2] School of Marine Science and Technology, Newcastle University, Newcastle upon Tyne, NE1 7RU, United Kingdom

[3] COTEC Offshore Engineering Solutions, Houston, Texas 77079, USA

Abstract

This article presents the research findings of an extensive model test investigation of the dynamic response to vortex-induced motions (VIMs) of the OC3 spar-type floating offshore wind turbine (FOWT). Particulars of this research are to investigate the unique and crucial effects of wind load on the spar-type FOWT, which differs considerably from other traditional spar-type floating systems utilized in the gas and oil industry, on the VIMs. The model test was performed with a sequence of current, wind and irregular wave sea states to analyze the nature of the coupled dynamic response behavior of VIMs. Many unique characteristics were found and analyzed. The lock-in phenomenon of sway in the cross flow (CF) direction was found to occur first, followed by the lock-in phenomenon of surge in the in-line (IL) direction. For the current-only case, the remaining responses, including the other 4-degree-of-freedom (DOF) motions, mooring tensions and turbine bearing loads, were found to be coupled by sway/surge VIMs. Moreover, the oscillation amplitudes of all of the responses increased significantly with increasing current velocity, particularly after locking-in. Furthermore, the wind load had a clear suppression effect on the CF and IL VIM responses. The experimental measurements demonstrated that the wave load excites wave-induced oscillations for some CF responses and all IL responses, and it further restrains the VIM oscillation amplitudes on the foundation of the wind suppression effect. In particular, when a wind load is involved, the influence of current or wave is limited to the yaw and IL tower-top bending moment.

Keywords: spar-type FOWT; vortex-induced motions; model test; dynamic response; suppression effect; coupling resonance

Nomenclature

VIM	vortex-induced motion
FOWT	floating offshore wind turbine
CF	cross flow
IL	in-line
CM	center of mass
TOML	tension of mooring line
PSD	power spectral density
LC	load case
Std	standard deviations
H_s	significant wave height
T_p	spectrum peak period
γ	spectrum peak factor
V_r	non-dimensional normalized current velocity

V_c	velocity of current
f_{st}	Strouhal frequency
f_v	vortex-shedding frequency
f_n	natural frequency of sway
D	diameter of the spar floater

1. Introduction

Research on floating offshore wind turbines (FOWTs) has developed rapidly and become of considerable interest in recent decades due to the increasing demand for energy and environmental protection concerns of the public. The research regarding FOWTs is multidisciplinary, involving aerodynamics, hydrodynamics, multi-structure dynamics (elastic) and automatic controls (servo).[1-4] Some studies have been performed by conducting a series of model tests on FOWTs.[5-10] Moreover, numerical simulation tools have been applied to conduct analyses in OC3 and OC4 projects,[11-14] and many simulation codes have been developed and improved for the fully coupled analysis of FOWT systems.[15-19] Among these studies, plenty of them have been performed regarding the spar-type FOWT concept due to its good hydrodynamic performance. However, a cylinder-type floater, such as the spar, exposed to a current load may experience alternate vortex shedding on both sides of the floater, resulting in periodic vortex-induced motions (VIMs), which may lead to the rapid accumulation of structural fatigue damage and an increased bearing load on the mooring system. Therefore, as the FOWTs have the tendency to be placed in deeper water, investigation of the dynamic responses of VIMs, particularly for spar-type FOWTs, becomes important. However, very few studies have been performed to investigate the VIM dynamic responses of the spar-type FOWT to date, and even fewer of them have been conducted using the model testing method.

The spar floater concept of FOWTs is derived from the spar-type oil offshore production platform, and extensive studies regarding VIMs have been performed on this oil offshore production platform, which provides a good research foundation for FOWTs supported by a spar-type floater. The model test method has been utilized worldwide to investigate VIM phenomena. Dijk et al.[20] performed a model test at the MARIN basin. The relative current velocity was simulated by dragging the model in calm water to investigate the characteristics of VIM responses for a truss spar. The reliability of predicting full-scale VIMs through model testing was verified. Van Dijk et al.[21] further conducted a model test comparing the VIM responses under various simulation methods of incoming current. One method was implemented by dragging the model in calm water, and the other was implemented by generating a current in the basin, respectively. Irani et al.[22] performed a 6-degree-of-freedom (DOF) model test with respect to the VIMs of a spar with a low Reynolds (Re) number, whereas Yung et al.[23] conducted a model test with a high Re number. Bybee[24] predicted the VIMs of a spar and investigated the fatigue response of the mooring system and riser under VIMs using various methods, such as theory analysis, model testing and prototype measurement. Oakley et al.[25] studied the VIMs of a classic spar in uniform current and shear current and investigated the simulation method of the stratified flow induced by a hurricane current or loop current. Irani et al.[26] performed a series of model tests to investigate the effectiveness of the strake design for a truss spar. Various designs of the strake were tested in this model test. Moreover, the strength and fatigue were considered, and corresponding modifications were presented. Thiagarajan et al.[27] compared the response characteristics of VIMs of bare and straked cylinders in uniform currents through computational fluid dynamics (CFD) analysis. The cylinder used in this research was identical to the hard tank part of the truss spar used in the model test conducted by Irani et al. in 2005. Atluri et al.[28] studied the effect of strake holes and surface appurtenances on the VIM responses of a truss spar using the CFD method and compared the results with those of the model test. Under various directions and velocities of the incoming current, the sensitivity level of the mesh and the turbulence simulation model were investigated with Re numbers ranging from 70,000 to 200,000.

Holmes[29] used CFD to simulate the VIM of a class spar in a uniform current which provides a suggestion for the model test based on this floating concept.

Although the FOWT with a spar-type floater has some common characteristics with the spar-type oil offshore production platform, it has a variety of unique features due to the significant portion supported by the floater, namely, the wind turbine. In contrast to the oil spar platform, in FOWTs, the effects of the wind load and the dynamic loads on the wind turbine are of great importance. A gyroscopic effect will be induced by the rotation of the rotor, which will notably affect the dynamic responses of the FOWT. How these factors influence the response of the FOWT undergoing VIM remains unclear up to now, and this paper is committed to make them clear. The basin test results are analyzed and discussed according to four main aspects:

1) Motion response characteristics under VIM
2) Dynamic characteristics of the mooring system under VIM
3) Dynamic characteristics of the turbine bearing loads under VIM
4) Effect of wind and wave loads on VIMs

Using the results of the model test conducted for VIMs in the spar-type wind turbine, this paper investigates the characteristics of the most dominant motion modes, namely, sway and surge, and other motion modes that are strongly influenced by sway and surge. Then, an analysis of the dynamic characteristics of VIMs on the mooring system is implemented based on various current velocities. The dynamic characteristics of loads on the wind turbine are investigated, mainly on the in-line (IL) and cross-flow (CF) tower-top shear force and bending moment, as well as the axial rotor thrust. Furthermore, the suppression of the wind load is investigated with regard to three aspects, namely, the restraining effect on the motions, mooring system and wind turbine bearing loads. Finally, the effect of wave on the FOWT under VIMs is also investigated.

2. Overview of the FOWT model test

The model test was conducted in the Deepwater Offshore Basin at Shanghai Jiao Tong University. A Froude number scaling ratio of 1:50 was selected, and a model water depth of 4 m was used to simulate a 200 m prototype value. The particular wind generation system was designed and fabricated to obtain a high-quality wind field.[30] The assembled spar-type FOWT model in the basin is shown in Fig. 1.

The model FOWT was geometrically scaled down from the OC3 project specifications, which were referenced by MARIN's basin test as well, and the main full-scale properties of the wind turbine are listed in Table 1.[11,12] In this table, CM indicates the center of mass, and the CM locations are calculated with respect to the still water level. In particular, the parameters of the modified floater and modified tower in Phase IV of the OC3 project[12] were utilized and are referred to as OC3-Hywind as well as the "OC3 Hywind tower" in this paper.

An image of the spar-type platform and its full-scale dimensional drawing[12] are shown in Fig. 2.

The taut mooring system utilized a delta connection to simulate the Hywind mooring type[9]. Fig. 3 shows the layout of the mooring system, where the bold circle represents the floater, the other lines are mooring lines, and the fairleads are located at the joints of two mooring lines. Additionally, three tension sensors were located at the joints of the two short mooring lines (lines B and C) to measure the tension of the mooring lines.

To accurately capture the coupled behaviour under simultaneous aerodynamic and hydrodynamic loading, it was important to design and build a wind generation system capable of providing a controllable wind field. The system developed for this research study is pictured in Fig. 4. It consisted of 9 independently controllable axial fans in a 3 x 3 stacked square configuration. The dimensions of the effective wind output area are 3.76 m times 3.76 m. The system can be used to generate model wind speeds up to 9.53 m/s. To enhance the wind environment quality for steady wind speeds, a honeycomb screen was attached to the front of the wind generation system.

A series of instruments were used to accurately capture the 6-DOF dynamic loads and 3-DOF accelerations of this FOWT system. The #1 load cell was connected between the nacelle and tower to measure the 6-DOF forces

and moments between them, and mainly to measure the IL/CF tower top shear force and bending moment. The #2 load cell was located in the nacelle to capture the 6-DOF forces and moments in the nacelle, and mainly to capture the rotor thrust force. The accelerometer was installed in the rear of the nacelle to measure the 3-DOF nacelle accelerations. The completed assembly configuration is shown in Fig. 5. In the experiment, a non-contact optical motion capture system was utilized to measure the 6-DOF motions of the floating system. The four active optical markers fixed at the end of the tower are shown in Fig. 6.

The definition of the 6-DOF motion based on the reference frame is shown in Fig. 7. The origin, *R*, of this reference coordinate system is located at the intersection of the tower centerline and the still water plane surface, where *RX* is oriented in the opposite direction of the wind, waves and current. Moreover, the 6-DOF forces and moments for the two load cells, as well as the 3-DOF accelerations, are also shown in Fig. 7. The wind, wave and current loads were always directed in 180° orientations during all basin tests.

Nine cases were defined, namely, cases with current-only, wind-only, wind with current, wind with wave and a combination of wind, wave and current, to investigate the VIM characteristics of the spar-type supported FOWT system. During this model test, the current environment was simulated as a uniform flow over the draft depth of the spar floater. The definitions of the load cases are given in Table 2. In this table, Hs, Tp and γ represent the significant wave height, spectrum peak period and spectrum peak factor, respectively. The wave condition in LC8 is selected from a one-year return period based on the Gulf of Maine[9]. The parameters of each load case are presented in both full scale and model scale.

3. Results and discussion

3.1 Investigation of the Wind field

The quality of the wind to be generated during the model test program was investigated using an array of DANTEC Dynamics MiniCTA anemometers with a 20 Hz sampling frequency. The array was designed to measure the time-series of the wind at forty-five measurement points and is illustrated in Fig. 8. As shown the array consisted of nine measurement points along the horizontal direction arranged at five different vertical elevations. This array was positioned 3 m downstream from the wind generation system based upon the typical distance between the floating wind turbine system and the wind generating system during the model basin testing. The objective was to characterize the spatial wind speed uniformity and the turbulence intensity in the near field of the spar-type floating wind turbine model.

The example of the approach used in the characterization of the wind field is shown in Fig. 9. The uniformity of the wind speed and the turbulence intensity are presented in Fig. 9 at model scale based on a targeted wind-making machine frequency of 7.2 Hz which represents the 23 m/s wind velocity load case.[31] Note that the model wind speed has been adjusted for achieving the desired thrust force under each wind speed condition, due to the lower Reynolds number for the model basin experiments.[31] The wind speed surface as shown represents the smoothed mean wind velocity values of the time histories, and the turbulence intensity surface is the corresponding temporal standard deviation of the time histories divided by the mean wind speed of the time history at each point in the grid.[32] The solid black circle is used to define the rotor plane in the wind field, and the black cross at its center indicates the positioning of the hub center at the x=1.88 m, y=1.506 m. As observed from these two figures, the spatial uniformity of the wind field is fair, and the turbulence intensity is generally lower than 22% within the rotor plane.

To further illustrate the variability of the wind field, a sample time history of the model wind speed at the 23rd measurement point is plotted in Fig. 10. This point was chosen because in the array it is the location closest to the hub center. Additionally, when exposed to this wind field (LC6), the time history of the axial rotor thrust (the foremost wind force) is also presented in Fig. 11.

Further, based on these two time histories of the wind speed and axial rotor thrust shown in Fig. 10 and Fig. 11, the power spectral densities (PSDs) are presented and analyzed in Fig. 12 and Fig. 13, respectively, to more clearly show the characteristics of the measured wind speed and to reveal the role that this wind file plays in the dynamic response behavior of the axial rotor thrust.

The curve of computed spectra in Fig. 12 shows a monotonically decreasing characteristic at low angular frequency because there exists a fluctuation with a long period and high amplitude in the time history, which also can be identified in Fig. 10. This characteristic results from the unsteadiness of the wind generation system and will have an influence on the motions or loads related to the wind load. Taking the response behaviour of axial rotor thrust in Fig. 13 as an example, the PSD result based on this wind-only load condition will also have a monotonically decreasing curve in the low frequency zone because of the low-frequency change property of the wind field. However, more important is, the axial rotor thrust response is dominated by the yaw-induced coupling resonance, which can be observed in Fig. 13 and will be described in detail in the following content.

3.2 Identification of the natural periods

Prior to the basin tests, free decay tests were conducted in calm water to identify the natural periods of the integrated FOWT system. The results of the free decay tests for the 6-DOF motions are listed in Table 3. All of the results of the model test will be presented based on the model scale.

3.3 Motion response characteristics under VIM

A spar-type floater will experience vortex shedding when exposed to a current flow. This vortex shedding procedure will mainly generate CF motion (sway) and IL motion (surge) based on the reference coordinate system defined in Fig. 7. Thus, the study of the VIMs will mainly focus on the surge and sway motion due to their importance. The amplitude of the oscillating motion in the CF direction due to vortex shedding is typically larger than that in the IL direction, and the CF motion is prone to resonate in a frequency identical to the natural frequency of the floating system over a rather broad range of normalized velocities, V_r ($=UT_n/D$), which is called the locked-in phenomenon. Therefore, the sway motion is critical for VIMs and will be analyzed in the most detail. The characteristics of the motion responses of the spar-type FOWT during VIMs are summarized in this section based on the analysis of the model test results.

Trajectory of vortex-induced surge and sway

To intuitively demonstrate the unique characteristics and the range of VIMs, Fig. 14 shows the trajectory of VIMs in one period based on the current-only case with a model velocity of 0.17 m/s.

As shown in this figure, the spar floater moves following the trajectory of a traditional ”figure-eight” during VIMs, as a smooth circular cylinder exposed to a homogeneous current flow typically does. Moreover, the range of the sway motion spans approximately 0.7 D, which is rather large, and the range of surge also spans approximately 0.5 D.

Identification of the vortex shedding frequency

The lift force on the cylinder oscillates at the vortex shedding frequency, implying that the vortex-shedding frequency is identical to the frequency of the exciting lift force. Additionally, the natural frequency will vary if the fluid environment is changed from still water to current flow, which will be explained in detail later. A comparison of Fig. 15 and Fig. 16 illustrates that for the case of Vc=0.042 m/s, the natural frequency in current is 1.051 rad/s, which is very close to the natural frequency in still water, namely 1.089 rad/s as listed in Table 3. This occurs because the difference in current velocity between this current environment of Vc=0.042 m/s and the still-water condition is relatively small if the still water is considered as a current flow with a velocity of zero. Therefore, the natural angular frequency in Fig. 15 drifts not far away from that in still water. However, for a relatively high

velocity, such as *Vc*=0.17 m/s, a significant difference exists in the current velocity between this current environment and the still-water condition, resulting in significant variations in the natural angular frequency, which shifts from 1.089 rad/s in still water to 0.759 rad/s in the current flow. Fig. 16 illustrates that in the lock-in range, the vortex-shedding angular frequency has been locked into the natural angular frequency (this point will also be explained later), namely 0.759 rad/s, which does not follow the Strouhal law anymore, causing the floating system to resonate in the sway direction near the natural period in current.

The response results of the sway during VIM are characterized by the following formula:

$$y = A_y \exp(-\frac{C_{sway}}{2m}t)\cos(w_d t) + A\cos(w_v t - \varphi) \quad (1)$$

where A_y is the amplitude of the first term from the damped free vibration, C_{sway} is the damping coefficient in the sway direction, m is the mass of the entire floating system, w_d is the sway natural angular frequency, A and φ are the amplitude and phase of the second term from the forced vibration, respectively, and w_v is the vortex-shedding angular frequency. Therefore, in Fig. 15, the floating system will oscillate with two angular frequencies. One is the natural angular frequency w_d (1.051 rad/s), and the other is the vortex-shedding angular frequency (0.314 rad/s). In this way, the vortex-shedding frequencies can be obtained from the power spectral density (PSD) of the sway responses.

Lock-in phenomenon

The relationship between the vortex-shedding frequency and sway natural frequency is one of the most important dynamic characteristics affecting the vortex-shedding motions. The characteristics of the lock-in procedure of sway are thoroughly characterized in Table 4 and Fig. 17.

In Fig. 17, V_r is the non-dimensional normalized current velocity, which is given by $V_r = \frac{UT_{n-sway}}{D}$, where U is the current velocity, $T_{n\text{-}sway}$ is the natural period of sway in still water, and D is the diameter of the spar floater. f_{st} is the Strouhal frequency, which is given by $f_{st} = St\frac{U}{D}$, where St is the Strouhal number (0.2, as listed in Table 4). f_v is the vortex-shedding frequency, and f_n is the natural frequency of sway that obtained from the free decay test results (0.173 Hz for the model scale, as listed in Table 3).

As shown in Fig. 17, the lock-in phenomenon can be clearly observed for a spar-type FOWT in the current condition. Before the normalized velocity value reaches 3.691, the vortex-shedding frequency will increase monotonously and follow the Strouhal frequency as the current velocity increases. However, with a further increase in the normalized velocity beyond this value of 3.691, the vortex-shedding frequency departs from the Strouhal frequency and begins to follow the natural frequency of the CF motion, namely, sway. It maintains this state over a rather broad range of V_r, causing a large resonance motion in the sway direction, which is known as the lock-in phenomenon. The lock-in phenomenon occurred during model testing based on load cases in the LC3, LC4 and LC5 conditions, as described in Table 4.

There is one point should be explained in Fig. 17 regarding the aforementioned variation of the natural frequency if the fluid environment is changed from still water to current flow. In Fig. 17, f_n is the natural frequency in still water and is obtained from the free decay in still water. However, the added mass in current may be larger than that in still water, resulting in a smaller natural frequency in current. For the ratio of f_v/f_n, if the f_n is used as the natural frequency in current, it will be the value of 1. But the f_n in Fig. 17 is used as the larger natural frequency in still water, so the ratio of f_v/f_n is smaller than unit, finally turned out to be 0.689.

Characteristics of sway and surge with various current velocities

Motion is the result of the corresponding exciting forces. Thus, the surge and sway during VIMs in the current-only cases are determined by the exciting lift and drag forces. The following content will demonstrate how current with various velocities influences the sway and surge responses. The PSDs of the sway and surge

responses based on five different velocities are shown in Fig. 18.

Fig. 18 illustrates that after lock-in, sway oscillates at the vortex-shedding angular frequency (0.759 rad/s), whereas the surge motion oscillates at approximately twice the vortex-shedding angular frequency (or twice the sway vibration angular frequency at lock-in, 1.68 rad/s). Furthermore, a comparison of these two diagrams in Fig. 18 illustrates that as the current velocity increases, the lock-in phenomenon of sway occurs first at *Vr*=3.691, and the lock-in phenomenon of the surge occurs subsequently at *Vr*=5.211. The oscillation amplitude of sway is larger than that of surge in each case, particularly after lock-in, due to the larger excitation of the oscillatory lift force. Additionally, the oscillation amplitudes of sway and surge will significantly increase as the current velocity increases, particularly after lock-in, which is an important point for designers. Take responses of the sway and surge based on *Vr*=5.211 (*Vc*=0.17) and *Vr*=6.079 (*Vc*=0.198), for instance, the increase in the model current velocity is only 0.028 m/s, however, the oscillation amplitudes increase by approximately three times for sway and 4.17 times for surge against a mere 16.5% increase in current velocity. This significant increase in the oscillation amplitude for sway and surge is dangerous for the floating system and should be considered in the design. However, comparing to this, there exists another key point that should be paid more attention to for the designers, that is the peak of the amplitude with various *Vr*. And this content will be discussed below. Besides, in particular, the vortex-induced surge and sway shown in Fig. 18 for the current-only case will cause resonant coupling responses to other motions or loads, and this point will be discussed later in detail.

A mean surge offset exists due to the non-zero mean drag force in response to a given current velocity. Fig. 19 shows in detail how the normalized mean surge and the normalized amplitude *A*/*D*, which is given by $A/D=(A_{\max}-A_{\min})/2D$, shift with the normalized velocity, V_r. D is the floater diameter. $A_{\max}$ and $A_{\min}$ are the maximum and minimum values of the time series, respectively.

As shown in Fig. 19, consistent with the response characteristics shown in Fig. 18, the surge and sway oscillation amplitudes both monotonously rise as the normalized velocity increases, and the VIM of the sway response, which is considerably larger than that of the surge, is nearly twice the surge response dimension in some current velocity cases due to the aforementioned larger excitation of the lift force. For the spar-floater concept used in this model test, the VIM phenomenon can be clearly observed, particularly at the relatively high normalized velocity, which should be a focus for the designer. The normalized amplitude, *A*/*D*, can reach approximately 0.8 D or even higher, thus the VIM will produce an enormous burden on the mooring system and should be considered. Additionally, the normalized mean surge also increases sharply with increases in V_r, particularly after lock-in, and can reach approximately 4 D. A large mean surge value will cause a large mooring tension in the IL direction and is unsafe for the mooring system. Particularly, it is also interesting to note that the increasing of the mean surge between two normalized velocities (V_r=2.171 and V_r=3.691) before lock-in appears a slow-down tendency relative to the overall increasing trend, implying the viscous mean drag force applied on the spar-type floater must also have the relevant slow-down increasing trend within this normalized velocity range.

Characteristics of other motions in various current velocities

The discussion above focuses on the most important VIMs, namely, sway and surge. As mentioned previously, the vortex-induced surge and sway will cause resonant coupling responses to other motions. Consequently, other components of the 6-DOF motions under various current velocities will be analyzed and discussed in this section based on the results of model tests to clearly identify the coupling effect from the surge/sway and to comprehensively examine the response characteristics of the VIMs. The attention is firstly paid to the motions that show clear resonant coupling induced by the sway VIM, due to the most prominent vortex-induced horizontal oscillation, namely sway. The PSD results of roll and yaw based on various current velocities are plotted in Fig. 20.

Fig. 20 illustrates that based on various current velocities, the roll motion oscillates at the resonant angular frequency of the sway VIM (or vortex-shedding angular frequency), indicating that the roll oscillation is excited by the sway VIM coupling. This occurs because the sway VIM causes the mooring system to generate a resultant

tension to restrain the sway VIM process in the CF direction, and this tension generates a moment with respect to the center of mass (CM) of the floating system, which finally induces the roll oscillation shown in Fig. 20. Consequently, the roll oscillations are inherently excited by the sway VIM, which is why the roll oscillates at the angular frequency of the sway VIM and has similar characteristics to those of the sway VIM shown in Fig. 18. Furthermore, based on each current velocity, the yaw motion mainly oscillates at two angular frequencies. One is completely identical to the angular frequency of the sway VIM, which is the resonant coupling induced by the sway VIM. Nevertheless, the other is basically identical to the angular frequency of the surge VIM, which can be considered the resonant coupling induced by the surge VIM. However, after lock-in, with a large amplitude oscillation of sway, the yaw motion will vibrate predominantly at the resonant angular frequency of the sway VIM, indicating that the yaw oscillation is mainly excited by the sway VIM in the current-only case. These sway/surge induced yaw oscillations are derived from the layout scheme of the mooring system (shown in Fig. 3) and consequently the dissymmetry of the mooring tensions during VIM processing. The oscillatory moment will be generated in the horizontal plane during VIM processing, which will finally cause the yaw oscillation.

The previous discussion focused on the sway-VIM coupled motions, and in the following, the responses that exhibit a resonant coupling with the surge VIM will be discussed. The PSD results of pitch and heave based on various current velocities are plotted in Fig. 21.

As shown in Fig. 21, the pitch motion oscillates at the resonant angular frequency of the surge VIM (or twice the vortex-shedding angular frequency), indicating that the pitch oscillation is excited by the surge VIM coupling for the current-only case. These pitch characteristics are induced for a similar reason as for the roll. The surge VIM causes the mooring system to generate a resultant tension to restrain the surge VIM process in the IL direction, and this tension generates a moment with respect to the CM of the floating system, which finally induces the pitch oscillation. In addition, the heave motion oscillates both at the resonant angular frequency of the sway and surge VIM. However, the oscillation induced by the surge VIM is dominant and considerably larger than that induced by the sway VIM, indicating that the heave oscillation is predominantly influenced by the surge VIM for the current-only case. Nevertheless, the reason of this phenomenon still needs a further in-depth investigation in future works. Moreover, all of the oscillation amplitudes of the aforementioned four motions as shown in Fig. 20 and Fig. 21, regardless of whether they are excited by the coupling effect of the sway VIM or surge VIM, increase significantly with increasing current velocity, particularly after lock-in.

To highlight the main VIMs, on which most attention should focused, the comparison of the response standard deviations for translational/rotational motions based on various current velocities was performed and is shown in Fig. 22.

As shown in Fig. 22, in the three modes of translational motion, the oscillation amplitudes of the surge and sway are approximately one more order of magnitude larger than that of the heave. In addition, the oscillation of sway is considerably larger than that of surge based on various current velocities, indicating that the sway oscillation is the most dominant mode among all of the vortex-induced translational motions. Moreover, Fig. 22 also shows that the oscillation responses of roll and pitch are considerably larger than that of yaw, implying that the rotational motions directly affected by the sway or surge VIM vibrate more severely. The maximum values of the response standard deviations for these three rotational motions are all lower than 1.2 degrees for various current velocities.

3.4 Dynamic characteristics of the mooring system under VIM

The mooring system will often bear large loads due to the VIM effect. The primary VIMs occur in the horizontal plane and are represented by reciprocating vibrations with large oscillation amplitudes, which may result in the peak value of the mooring tension. The peak value of the mooring tension is the key parameter for designing and controlling the breaking strength of the mooring system. In addition, repeated periodic exciting

loads may also cause fatigue of the mooring system. Therefore, the mooring system will be most negatively affected by the VIM. How the mooring system responds under various current velocities is critical for the safety of the floating system and will be discussed in detail in this chapter based on the results of model tests. As noted above, three tension sensors were located at the joints of the two short mooring lines (lines B and C) to measure the tensions on the mooring lines, which are shown in Fig. 3. The tension of mooring line 2 (TOML2) was selected as the representative mooring tension due to the symmetry of the TOML1 and TOML2, as shown in Fig. 3. The PSD results of the TOML2 and TOML3 based on various current velocities are plotted in Fig. 23.

A comparison of Fig. 18 and Fig. 23 illustrates that the oscillation angular frequency of the TOML2 is identical to that of the sway VIM (or vortex-shedding angular frequency) based on each current velocity, and the oscillation characteristics of the TOML2 and sway VIM are approximately the same, indicating that the vibration of the TOML2 is predominantly determined by the sway VIMs. Nevertheless, the oscillation angular frequency of the TOML3 is identical to that of the surge VIMs (or twice the vortex-shedding angular frequency) based on each current velocity, and the oscillation characteristics of the TOML3 are highly similar to that of the surge, indicating that the vibration of the TOML3 is predominantly determined by the surge VIMs. Fig. 23 also shows that with increasing current velocity, the oscillation amplitudes of the TOML2 and TOML3 both increase, particularly after locking-in. The oscillation amplitude increases substantially, which significantly burdens the mooring system and greatly compromises the safety of the mooring system. Furthermore, because the vibrations of the TOML2 and TOML3 are predominantly determined by the sway and surge, respectively, the oscillation angular frequency of the TOML2 is approximately twice that of the TOML3 because the oscillation angular frequency of sway is approximately twice of that of the surge. In addition, the oscillation amplitude of the TOML2 is considerably larger than that of the TOML3 due to the considerably larger oscillation amplitude of the sway compared to that of the surge.

As mentioned previously, the non-zero mean drag force will produce a mean surge in the IL direction, which will cause a mean offset in the TOML2 and TOML3. The mean surge increases with increasing current velocity, resulting in an increase in the mean offset of the TOML2 while a decrease in the mean offset of the TOML3. Fig. 24 shows how the mean offset and maximum values of the TOML2 and TOML3 vary with the normalized velocity V_r.

When no current is present in the fluid environment, the TOML2 and TOML3 will be equal to 21.56 N, which is the pretension of each mooring line. However, when a current with velocity of 0.042 m/s is present in the fluid field, the mean TOML2, as shown in Fig. 24, will change to 21.808 N, whereas the mean TOML3 will shift to 21.061 N due to the mean surge offset. Subsequently, the mean surge increases with increasing current velocity, resulting in an increase in the mean offset of the TOML2 and a decrease in the mean offset of the TOML3, as shown in Fig. 24. This diagram also illustrates that the mean offset of the TOML3 decreases significantly as the normalized current velocity increases, particularly in the lock-in range, which is derived from the variation characteristics of the mean surge, as shown in Fig. 19. However, the increasing trend of the mean offset of the TOML2 is relatively gentle compared to the decreasing trend of the mean offset of the TOML3. Additionally, because mooring line 2 endures considerably more stretch load than mooring line 3, mooring line 2 (or mooring line 1) is in the most danger and the TOML2 (or TOML1) should be the principle concern. Fig. 24 shows that with increasing current velocity, the mean TOML2 can reach 24.007 N or even greater. The VIM will produce large amplitude motions predominantly in the horizontal plane, resulting in a large peak value of mooring tensions. The extent of the mooring tension during VIM is crucial for the safety of the mooring system and deserves considerable attention.

As shown in Fig. 24, with increasing normalized current velocity, the maximum TOML2 increases, whereas the maximum TOML3 decreases. Moreover, the maximum TOML2 increases significantly as normalized current velocity increases, particularly in the lock-in range. Furthermore, the increasing trend of the maximum TOML2 is

more severe than the decreasing trend of the maximum TOML3. This trend occurs because the oscillation of the TOML2 is predominantly induced by the sway VIM, whereas the oscillation of the TOML3 is mainly induced by the surge VIM, as noted previously, and the oscillations of the sway and surge both increase with increases in normalized current velocity. In addition, the vibration amplitude of the sway during VIM is considerably larger than that of the surge, resulting in a more drastic variation trend of the maximum TOML2 and a considerably larger maximum TOML2 compared to the TOML3. The maximum TOML2 can reach 36.259 N or even larger.

3.5 Dynamic characteristics of turbine bearing loads under VIM

In contrast to other traditional spar-type oil offshore systems, the bearing loads on the wind turbine are unique and crucial for the FOWT system. The dynamic characteristics of turbine bearing loads for the spar-type FOWTs are analyzed in this section based on the model test results. The vortex-induced sway/surge oscillations will cause resonant coupling to bearing loads, as noted above. Consequently, how the corresponding loads are influenced by the VIMs, mainly the sway and surge, is of great importance. For the FOWT system, the axial rotor thrust, tower-top shear force and tower-top bending moment are always the most significant parameters because they are highly related to the structural safety of the entire floating system. Therefore, the analysis in this section will focus on these parameters. As shown in Fig. 7, the IL/CF tower-top shear force and bending moment are measured by the #1 load cell and labeled Fx1, Fy1, My1 and Mx1, respectively. The axial rotor thrust is measured by the #2 load cell and is labeled Fx2.

Similar to the discussion sequence of motion responses, the bearing loads that have resonant coupling induced by sway will be analyzed and discussed first. The PSD results of the CF tower-top shear force and bending moment are plotted in Fig. 25.

As shown in Fig. 25, the CF tower-top shear force and bending moment have similar dynamic characteristics. They predominantly oscillate at the resonance angular frequency of the sway VIM, indicating that the oscillations of these two loads are both predominantly excited by the sway VIM.

The responses that show resonant coupling with the surge VIM will be discussed below. The PSD results of the IL tower-top shear force and bending moment, as well as the axial rotor thrust, are plotted in Fig. 26 based on various current velocities. Nevertheless, due to the manufacturing and installation requirements, the data of rotor thrust collected in this model test is not the thrust force applied directly to the hub, but rather contains the inertial force induced by the motor installed in front of the load cell. Regardless, the test data can still reflect the major dynamic characteristics of the thrust force.

Fig. 26 indicates that, the IL tower-top shear force and bending moment, as well as the axial rotor thrust have similar dynamic characteristics. Based on each current velocity, these parameters oscillate at the resonance angular frequency of the surge VIM and have rather similar characteristics to those of the surge VIM shown in Fig. 18, indicating that the oscillations of these three loads are excited by the surge VIM. In addition, Fig. 26 illustrates that the oscillation amplitude of the axial rotor thrust is smaller than that of the IL tower-top shear force. This trend occurs because the inertial component of the IL tower-top shear force is due to the entire mass of the nacelle and rotor. However, the inertial component of the axial rotor thrust is only due to the mass of the rotor and the motor located behind the rotor, which is lighter than the previous mass, resulting in a smaller inertial force and thus a smaller oscillation amplitude. Fig. 25 and Fig. 26 indicate that the oscillation amplitudes of these five bearing loads increase significantly with increasing current velocity, particularly after locking-in, regardless of whether they are excited by the coupling effect of the sway VIM or surge VIM. In addition, the oscillation amplitude of the IL tower-top shear force and the bending moment are considerably larger than those of the CF, implying that the wind turbine bearing loads in the IL direction are more harmful to the safety of the floating system for the current-only case.

3.6 Effect of wind and wave loads on VIMs

For an offshore structure, such as an FOWT, wind and wave are significant important exciting loads. An FOWT subjected to a combined effect of wind, wave and current represents a typical situation in a sea environment. Consequently, the roles of the wind and wave loads on a FOWT exposed to current loads should be examined and will be discussed in this chapter based on the results of model tests. As discussed previously, the responses, such as motions, mooring tensions and bearing loads, all have a coupling effect either induced by the sway VIM or surge VIM for the current-only case. Besides, the model test demonstrated that the yaw motion is dominated by the rotor rotation and the yaw motion reflects some clear coupling effects to other responses, even rather significant for some particular responses. Therefore, the discussion will be oriented toward three aspects that focus on the CF responses (sway and responses closely related to sway), IL responses (surge and responses closely related to surge) and responses that are closely related to rotor rotation (or yaw motion).

Inhibition effects on the CF responses

The response in the CF direction is of particular interest due to its largest oscillation amplitude and potential threat to the safety of the mooring system. Consequently, the influences of wind and wave on the CF responses will first be analyzed and discussed in this section. The PSD results of sway and the TOML2 based on LC4, LC7 and LC9 are plotted in Fig. 27.

Because the TOML2 is closely related to sway motion and its oscillation is approximately determined by the sway VIM in current-only case, the characteristics of the TOML2 are highly similar to those of the sway. The diagram clearly indicates that for both sway and TOML2, the wind load does not shift the vortex-shedding induced resonant angular frequency, whereas it restrains the VIMs to a large extent. The oscillations of sway and TOML2 under the wind and current condition are both reduced to approximately half of those in the current-only condition. Additionally, since the directions of the incoming wind, wave and current are identical as shown in Fig. 7, the influence of the wave on the CF motion, namely sway, subsequently on the response of the TOML2, is limited and basically not cause a resonant responses at the wave angular frequency for both the sway and TOML2, as shown in Fig. 27. Moreover, as the wind load does, the wave load does not change the resonant angular frequency of the sway and subsequently the TOML2 as well. In other words, the sway motion and TOML2 will always oscillate at the vortex-shedding angular frequency (0.759 rad/s), regardless of whether the load environment is the current only, wind with current or combined wind, wave and current condition, when the floating system is under the lock-in condition. However, the oscillation amplitude of sway (or TOML2) based on load case of combined wind, wave and current (LC9) is approximately half of that in the wind with current load case (LC7) and approximately one quarter of that in the current only load case (LC4). This finding indicates that the wave load further restrains the VIM of the sway and the oscillation of TOML2 on the foundation of the suppression effect from the wind load. To comprehensively demonstrate the response characteristics, time histories of sway based on LC4, LC7 and LC9 are additionally overlaid in Fig. 28 as a typical example. Next, the PSD results of roll based on LC4, LC7 and LC9 are plotted in Fig. 29 and will be analyzed below.

As shown in Fig. 29, because the roll oscillation is determined by the sway VIM for the current-only case, the oscillation of roll for the wind with current case is clearly restrained by the wind load due to the prominent suppression of the wind load on the sway VIM, as shown in Fig. 27. In addition, a yaw-induced resonant coupling response of roll is present (which will be explained later), although it is extremely small, implying the existence of a coupling effect between roll and yaw. Besides, for the combined wind, wave and current case, the wave load further restrains the oscillation of roll at the resonant angular frequency of the sway VIM to some extent on the foundation of the suppression effect from the wind load, and excites the oscillation at the roll natural frequency. The yaw-coupled resonant response still exists but the incoming wave also does not excite the wave-frequency resonance of roll. The PSD results of the CF tower-top shear force and bending moment based on LC4, LC7 and LC9 are plotted in Fig. 30.

Fig. 30 shows that the characteristics of the CF tower-top shear force are highly similar to those of the CF

tower-top bending moment. When wind load is involved, the oscillations of the CF tower-top shear force and bending moment, at the angular frequency of the sway VIM, are clearly restrained by the wind load and are less than half of those for the current-only case. In addition, the wind load also produces a coupling effect of the yaw to these two loads, causing these two oscillation components induced by sway-VIM and yaw-coupling to be of the same order of magnitude. When experiencing the combined effect of wind, wave and current, the wave load further restrains the oscillation at the angular frequency of the sway VIM on the foundation of the suppression effect from wind load and excites the oscillations at the roll natural frequency for these two responses, implying that the roll motion will bring coupling effect on these two loads under the combined wind, wave and current condition. Moreover, the coupling resonance induced by yaw motion is basically not changed by the wave load for either the CF tower-top shear force or bending moment. Furthermore, the wave load excites the oscillation of these two loads at the wave angular frequency based on LC9. The oscillations of the CF tower-top shear force and bending moment totally consist of four components, that are respectively contributed by sway VIM, roll natural angular frequency, incoming wave and coupling effect of yaw, and these four components are mainly on the same level.

Effects on the IL responses

The IL direction is the direction of the incoming wind, wave and current, due to which the large amplitude oscillations of motions and loads may be caused. Consequently, how the IL motions and loads respond in the wind with current and combined wind, wave and current sea environments deserve attention and will be discussed in this section. The PSD results of the surge and pitch based on LC4, LC7 and LC9 are plotted in Fig. 31.

As shown in Fig. 31, the characteristics of surge motion are similar to those of pitch. The wind load transfers both the oscillation angular frequencies of surge and pitch from the vortex-shedding induced resonant angular frequency to the surge/pitch natural angular frequency. Oscillations of surge and pitch are both extremely restrained due to the wind load. The incoming wave further restrains the oscillation components of surge and pitch at the surge/pitch natural angular frequency on the foundation of the suppression effect from the wind load, nevertheless, the suppression effect of wave is relatively limited. Furthermore, the incoming wave produces the resonance of surge and pitch at the wave angular frequency. However, the aforementioned extreme suppression due to the wind load reduces the oscillation response of the surge/pitch at the surge/pitch natural angular frequency to a large extent, causing the oscillation component at the wave angular frequency to be the dominant component. This suppression effect implies that in the current-only load case (LC4), the incoming current is the crucial exciting contributor to the surge/pitch oscillation. However, in the load case of combined wind, wave and current (LC9), the incoming wave, rather than the current, becomes the dominant exciting contributing factor to the oscillation. In addition, time histories of surge (as the typical response) based on these three load cases are overlaid in Fig. 32 for a supplementary understanding. Next, the PSD results of the TOML3 and heave motion based on LC4, LC7 and LC9 are plotted in Fig. 33.

Fig. 33 shows that the wind load also transfers the oscillation angular frequency from the resonant angular frequency induced by surge VIM coupling to the natural angular frequency. However, unlike the suppression of the wind load on the surge VIM shown in Fig. 31, in which the surge oscillation is reduced to an extremely small value, the suppression effect of the wind load on the vibration of the TOML3 is relatively limited. Nevertheless, the reason of this phenomenon still needs a further in-depth investigation in future works. However, it is worth noting that the suppression on the VIM is not the only influence produced by the wind load. It will also cause insecurity of the mooring system as well, as described below. The statistics of mooring line tensions based on the current-only and wind with current load cases are shown in Table 5.

Table 5 illustrates that the wind load increases the mean surge, implying that the floating system is pushed to a farther IL equilibrium position by the wind load, resulting in larger mean mooring tensions of mooring lines 1 and 2. Although the suppression of VIM due to the wind load is advantageous for the floating and mooring

systems, the burden of the mooring system is actually increased, particularly for mooring lines 1 and 2. This occurs because the maximum values become larger based on this wind with current case, which will challenge the breaking-tension of mooring lines 1 and 2 and will compromise the security of the mooring system.

For heave responses in Fig. 33, the wind load restrains the vibration at the resonant angular frequency of the sway VIM to some degree, however, it significantly restrains the vibration at the resonant angular frequency of the surge VIM due to the extreme suppression effect of wind load on the surge VIM.

Additionally, it also can be identified from Fig. 33 that the incoming wave produces oscillation of the TOML3 and heave at the wave angular frequency. Besides, the wave load further restrains the oscillation component of the TOML3 at the surge/pitch natural angular frequency to approximately half of the oscillation amplitude based on the current-only case. However, the wave load re-excites the oscillation component of heave at the resonant angular frequency of the surge VIM, causing the oscillation component at this angular frequency of the surge VIM based on LC9 to be considerably larger than that based on the wind with current case and clearly smaller than that based on the current-only case. Nevertheless, the oscillation amplitude of heave is extremely small compared to the responses of other motions and loads. The PSD results of IL tower-top shear force and axial rotor thrust based on LC4, LC7 and LC9 are plotted in Fig. 34.

As shown in Fig. 34, the characteristics of IL tower-top shear force are highly similar to those of axial rotor thrust. Due to the close coupling of these two responses with the surge VIM in the current-only case, the wind load also transfers the oscillation angular frequency from the resonant angular frequency induced by surge VIM coupling to the natural angular frequency and extremely restrains the oscillation amplitude both for these two responses, similar to the manner in which the wind load influences the surge VIM in Fig. 31. Furthermore, the wave load excites the oscillation component of the IL tower-top shear force and axial rotor thrust at the wave angular frequency, which is dominant based on LC9 and even higher than that excited by the surge VIM in the current-only case (LC4), implying that in LC4, the incoming current is the crucial exciting contributor to the oscillations. However, in the load case of wind, wave and current (LC9), the incoming wave, rather than the current, becomes the dominant exciting contributor to the oscillations.

Effects on the yaw and its closely related responses

The yaw response is rather unique compared to other motions, reflecting its near independence from the sway/surge coupling with a unique dependence on rotor rotation when wind load is involved, which will be discussed later. In addition, this rotation-excited yaw will produce a clear coupling effect to other responses (such as roll, CF tower-top shear force and bending moment, as noted above) and the coupling effect can be rather significant for some particular responses (such as IL tower-top bending moment, which will be mentioned below). The PSD results of yaw and the IL tower-top bending moment based on LC4, LC7 and LC9 are plotted in Fig. 35.

Fig. 35 shows that regardless of whether the external fluid environment consists of wind with current or combined wind, wave and current, the yaw motion always predominantly oscillates at the angular frequency induced by the gyroscopic effect of the rotor rotation, basically neither reflects the sway/surge induced oscillation nor the wave-excited oscillation, indicating that once the wind load is involved (inherently rotor rotation occurs), the yaw oscillation is mainly determined by the rotor rotation and is relatively independent from the incoming current and wave. Fig. 35 also shows that in the wind with current and combined wind, wave and current load cases, the IL tower-top bending moment predominantly depends on the yaw motion, which is represented by the dominant oscillation amplitude at the resonant angular frequency of yaw coupling. Furthermore, the vibration excited by the surge VIM is extremely restrained by the wind load, and the wave load produces the oscillation component at the wave angular frequency, but relatively limited. Besides, for an intuitional presentation of this particular yaw response, time histories based on LC4, LC7 and LC9 are overlaid in Fig. 36 as a supplement.

4 Conclusions

A model test of a spar-type FOWT was performed to investigate the dynamic characteristics of the spar-type FOWT during VIM and provide verification materials for FOWT simulation codes. The following conclusions can be drawn:

1) The lock-in phenomenon occurs at the normalized current velocity of 3.691. The lock-in phenomenon of sway occurs first, followed by the lock-in phenomenon of surge, and the oscillation amplitude of sway is considerably larger than that of surge. For the current-only condition, the oscillations of roll and yaw are predominantly excited by sway VIM coupling, whereas the oscillations of pitch and heave are predominantly excited by surge VIM coupling. Moreover, all of the oscillation amplitudes of the 6-DOF motions are significantly increased with increasing current velocity, particularly after locking-in.
2) In the current-only case, the vibrations of the TOML2 and TOML3 are predominantly determined by the sway and surge VIM, respectively. Moreover, with increasing current velocity, the oscillation amplitude of the TOML2 and TOML3 both increase, and the mean offset and maximum value of TOML2 increase, whereas the mean offset and maximum value of TOML3 decrease due to the layout of the mooring system. In particular, when the current velocity increases, the increasing trend of the mean offset of the TOML2 is relatively gentler than the decreasing trend of the mean offset of the TOML3, whereas the increasing trend of the maximum TOML2 is sharper than the decreasing trend of the maximum TOML3.
3) Under the current-only condition, the CF tower-top shear force and bending moment are predominantly excited by the sway VIM coupling and have similar dynamic characteristics. Moreover, the IL tower-top shear force and bending moment, as well as the axial rotor thrust, are excited by the surge VIM coupling and have similar dynamic characteristics. The oscillation amplitudes of bearing loads increase significantly with increasing current velocity, particularly after locking-in. In addition, the wind turbine bearing loads in the IL direction are more harmful to the safety of the floating system due to considerably larger oscillation amplitudes in the current-only case.
4) The wind load basically does not shift the vortex-shedding-induced resonant angular frequency of the sway, whereas it restrains the VIM to a large extent. However, the wind load highly restrains the oscillation of surge, pitch, IL tower-top shear force and axial rotor thrust, as well as the surge VIM-induced resonant component of heave. The oscillations of roll, TOML2, CF tower-top shear force and bending moment are also clearly restrained by the wind load. Nevertheless, the suppression effect of the wind load on the vibration of the TOML3 is relatively limited. When wind load is involved, the oscillation of the yaw is predominantly excited by rotor rotation, and the IL tower-top bending moment is predominantly excited by rotation-induced yaw, causing these two responses to be largely independent from the coupling effect of the vortex-induced sway/surge motions.
5) The wave load further restrains the VIM oscillation amplitudes of CF responses on the foundation of the wind suppression effect and excites the wave-induced oscillation for CF tower-top shear force and bending moment, but the suppression effect is limited. Moreover, the yaw coupling resonant components of the CF responses are mainly not influenced by the incoming wave. Furthermore, for IL responses, the incoming wave further restrains the oscillation components at natural angular frequencies on the foundation of the wind suppression effect, whereas it re-excites the surge-VIM-coupled oscillation component of heave and excites wave-induced oscillations. The amplitudes of this wave-excited oscillation for some responses can become extremely large and dominant. However, the influence of wave on the yaw and IL tower-top bending moment is also limited, similar to the influence of current on these two responses, when a wind load is involved.

Acknowledgements

The authors would like to acknowledge the SKLOE (State Key Lab of Ocean Engineering) in Shanghai Jiao

Tong University for model testing research support. The financial support from the Natural Science Fund of China (Grant No. 51239007) is also gratefully acknowledged by the authors.

References

[1]H. Namik, K. Stol, "Individual Blade Pitch Contorl of Floating Offshore Wind Turbines", Wind Energy **13**(1), 74-85 (2010).

[2]L. Wang, B. Sweetman, "Multibody dynamics of floating wind turbines with large-amplitude motion", Applied Ocean Research **43**, 1-10 (2013).

[3]M. Jeon, S. Lee, S. Lee, "Unsteady Aerodynamics of Offshore Floating Wind Turbine in Platform Pitching Motion Using Vortex Lattice Method" Renewable Energy **65**, 207-212 (2014).

[4]S. Salehyar, Q. Zhu, "Aerodynamic dissipation effects on the rotating blades of floating wind turbines", Renewable Energy **78**, 119-127 (2015).

[5]F. G. Nielsen, T. D. Hanson, B. Skaare, "Integrated Dynamic Analysis of Offshore floating Wind Turbines", in *Proceedings of 25th International Conference on Offshore Mechanics and Arctic Engineering*, Hamburg, Germany, 4-9 June 2006 Paper no. OMAE2006-92291.

[6]H. Shin, "Model Test of the OC3-Hywind Floating Offshore Wind Turbine", in *Proceedings of the Twenty-first (2011) International Offshore and Polar Engineering Conference*, Maui, Hawaii, USA, 19-24 June 2011 (ISOPE, 2011).

[7]C. Cermelli, A. Aubault, D. Roddier, T. McCoy, "Qualification of a Semi-Submersible Floating Foundation for Multi-Megawatt Wind Turbines", *Offshore Technology Conference*, Houston, Texas, USA, 3-5 May 2010. Paper no. OTC 20674

[8]H. R. Martin, R. W. Kimball, A. M. Viselli, A. J. Goupee, "Methodology for Wind/Wave Basin Testing of Offshore floating Wind Turbines", in *Proceedings of the ASME 2012, 31st International Conference on Ocean, Offshore and Arctic Engineering*, Rio de janeiro, Brazil, 1-6 July 2012. Paper no. OMAE2012-83627.

[9]B. Koo, A. J. Goupee, K. Lambrakos, R. W. Kimball, "Model Tests for a Floating Wind Turbine on Three Different Floaters", in *Proceedings of the ASME 2012, 31st International Conference on Ocean, Offshore and Arctic Engineering*, Rio de janeiro, Brazil, 1-6 July 2012. Paper no. OMAE2012-83642.

[10]A. J. Goupee, B. Koo, R. W. Kimball, K. F. Lambrakos, H. J. Dagher, "Experimental Comparison of Three Floating Wind Turbine Concepts", in *Proceedings of the ASME 2012, 31st International Conference on Ocean, Offshore and Arctic Engineering*, Rio de janeiro, Brazil, 1-6 July 2012. Paper no. OMAE2012-83645.

[11]J. Jonkman, S. Butterfield, W. Musial, G. Scott, "Definition of a 5-MW Reference Wind Turbine for Offshore System Development" Technical Report NREL/TP-500-38060, NREL, Golden, Colorado, USA, February 2009

[12]J. Jonkman, "Definition of the Floating System for Phase IV of OC3", Technical Report NREL/TP-500-47535, NREL, Golden, Colorado, USA, May 2010.

[13]J. Jonkman, A. Robertson, W. Popko, F. Vorpahl, A. Zuga, M. Kohlmeier, T.J. Larsen, A. Yde, K. Saetertro, K.M. Okstad, J. Nichols, T.A. Nygaard, Z. Gao, D. Manolas, K. Kim, Q. Yu, W. Shi, H. Park, A.V. Rojas, J. Dubois, D. Kaufer, P. Thomassen, M.J. de Ruiter, J.M. Peeringa, H. Zhiwen, H.V. Waaden, "Offshore Code Comparison Collaboration Continuation (OC4), Phase I – Results of Coupled Simulations of an Offshore Wind Turbine with Jacket Support Structure", NREL/CP-5000-54124, 22nd International Society of Offshore and Polar Engineers Conference, Rhodes, Greece, 2012.

[14]A. Robertson, J. Jonkman, W. Musial, F. Vorpahl, W. Popko, "Offshore Code Comparison Collaboration, Continuation: Phase II Results of a Floating Semisubmersible Wind System", NREL Technical Report, NREL/CP-5000-60600, November 2013.

[15]M. Karimirad, "Stochastic Dynamic Response Analysis of Spar-Type Wind Turbines with Catenary or Taut Mooring Systems", Ph.D. Thesis, Norwegian University of Science and Technology, 2011.

[16]M. I. Kvittem, E. E. Bachynski, T. Moan, "Effects of Hydrodynamic Modeling in Fully Coupled Simulations of a Semisubmersible-Submersible Wind Turbine", Energy Procedia **24**, 351-362 (2012).

[17]S. Quallen, T. Xing, P. Carrica, Y. W. Li, J. Xu, "CFD Simulation of a Floating Offshore Wind Turbine System Using a Quasi-Static Crowfoot Mooring-Line Model", in *Proceedings of the Twenty-third (2013) International Offshore and Polar Engineering*, Anchorage, Alaska, USA, 30 June-5 July 2013 (ISOPE, 2013).

[18]Y. H. Bae, M. H. Kim, Y. S. Shin, "Rotor-floater-mooring Coupled Analysis of Mini-TLP-Type Offshore Floating Wind Turbines", in *Proceedings of the ASME 2010 29th International Conference on Ocean, Offshore and Arctic Engineering*, Shanghai, China, 6-11 June 2010. Paper no. OMAE2010-20555.

[19]S. Gueydon, W. Xu, "Floating Wind Turbine Motion Assessment", *Oceans11 Conference*, Kona, Hawaii, USA, 19-22 September 2011.

[20]R.V. Dijk, A. Magee, S.V. Perryman, J.V. Gebara, "Model test experience on Vortex Induced Vibrations of Truss Spars", *Offshore Technology Conference*, Houston, Texas, USA, 5-8 May 2003.

[21]R.R.T. van Dijk, A. Voogt, P. Fourchy, S. Mirza, "The effect of mooring system and sheared currents on vortex induced motions of truss Spars" in *Proceedings of the 22ND International Conference on Offshore Mechanics and Arctic Engineering*, Cancun, Mexico, 8-13 June 2003. Paper no. OMAE2003-37151.

[22]M. Irani, L. Finn, "Model testing for vortex induced motions of spar platforms", in *Proceedings of the 23rd International Conference on Offshore Mechanics and Arctic Engineering*, Vancouver, British Columbia, Canada, 20-25 June 2004. Paper no. OMAE2004-51315.

[23]T. W. Yung, R.E. Sandström, S. T. Slocum, Z. J. Ding, R. T. Lokken, "Advancement of Spar VIV Prediction", *Offshore Technology Conference*, Houston, Texas, USA, 3-6 May 2004.

[24]K. Bybee, "Spar vortex-induced-vibration prediction", Journal of Petroleum Technology **57**(2), 61-63 (2005).

[25]Jr. O. H. Oakley, Y. Constantinides, C. Navarro, S. Holmes, "Modeling vortex induced motions of spars in uniform and stratified flows", in *Proceedings of the 24th International Conference on Offshore Mechanics and Arctic Engineering*, Halkidiki, Greece, 12-17 June 2005. Paper no. OMAE2005-67238.

[26]M. Irani, L. Finn, "Improved strake design for vortex induced motions of spar platforms", in *Proceedings of the 24th International Conference on Offshore Mechanics and Arctic Engineering*, Halkidiki, Greece, 12-17 June 2005. Paper no. OMAE2005-67384.

[27]K. P. Thiagarajan, Y. Constantinides, L. Finn, "CFD analysis of vortex-induced motions of bare and straked cylinders in currents", in *Proceedings of the 24th International Conference on Offshore Mechanics and Arctic Engineering*, Halkidiki, Greece, 12-17 June 2005. Paper no. OMAE2005-67263.

[28]S. Atluri, J. Halkyard, S. Sirnivas, "CFD simulation of Truss Spar Vortex-Induced Motion", in *Proceedings of the 25th International Conference on Offshore Mechanics and Arctic Engineering*, Hamburg, Germany, 4-9 June 2006. Paper no. OMAE2006-92400.

[29]S. Holmes, "Predicting Spar VIM Using CFD", in *Proceedings of the ASME 27th International Conference on Offshore Mechanics and Arctic Engineering*, Estoril, Portugal, 15-20 June 2008. Paper no. 2008-57706.

[30]F. Duan, Z. Q. Hu, J. Wang, "Model Tests of a Spar-type Floating Wind Turbine under Wind/Wave Loads", in *Proceedings of the ASME 2015, 34th International Conference on Ocean, Offshore and Arctic Engineering*, St. John's, NL, Canada, 31 May-5 June 2015. Paper no. OMAE2015-41391.

[31]F. Duan, Z. Q. Hu, J. M. Niedzwecki, "Model test investigation of a spar floating wind turbine", Marine Structures **49**, 76-96 (2016).

[32]M. J. Fowler, R. W. Kimball, D. A. Thomas III, A. J. Goupee, "Design and testing of scale model wind turbines for use in wind/wave basin model tests of floating offshore wind turbines", in *Proceedings of the ASME 2013 32nd International Conference on Ocean, Offshore and Arctic Engineering*, Nantes, France, 9-14 June 2013. Paper no. OMAE2013-10122.

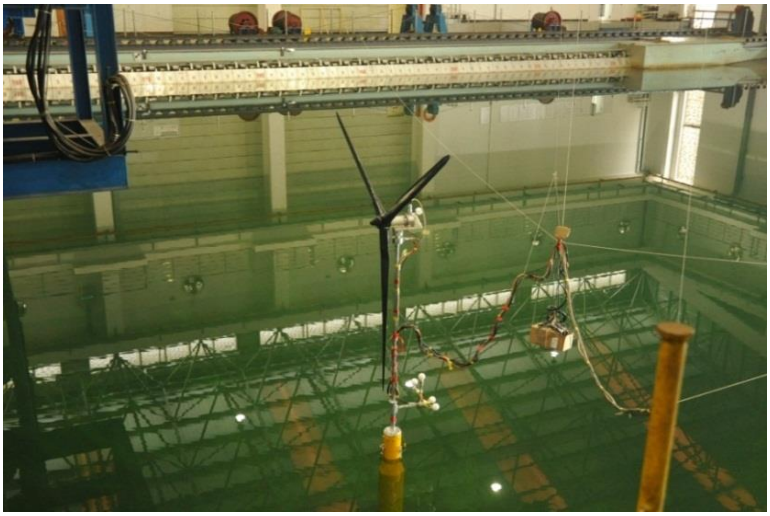

Fig. 1 FOWT model in the basin

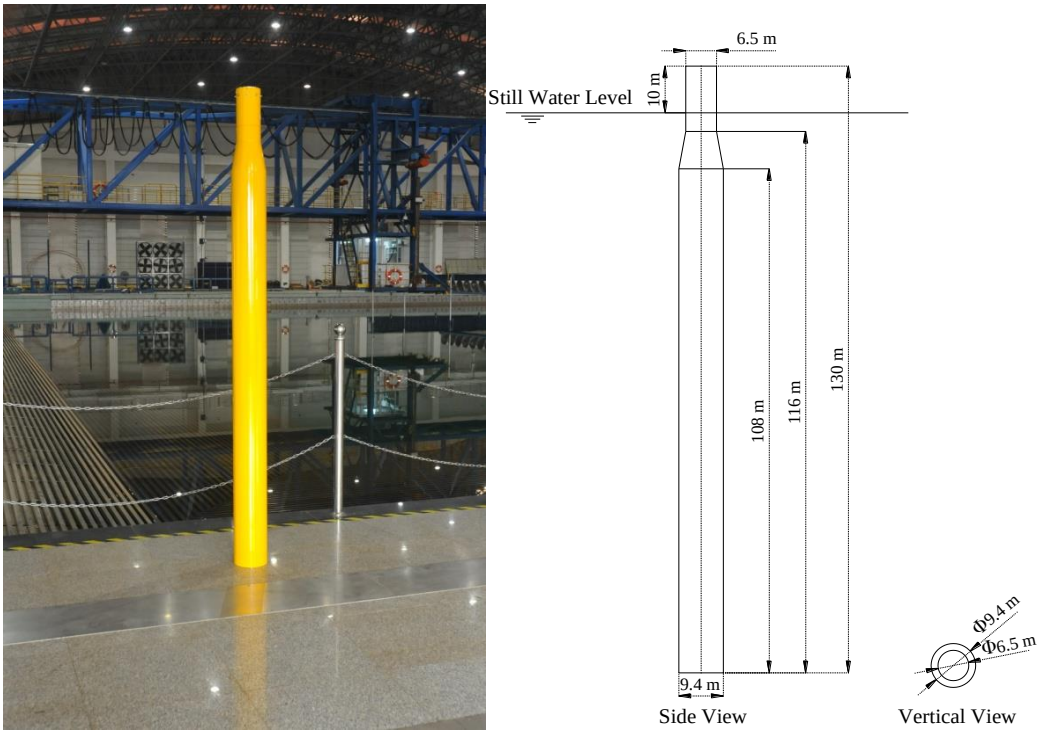

Fig. 2 Photograph and main dimensions of the spar-type floater

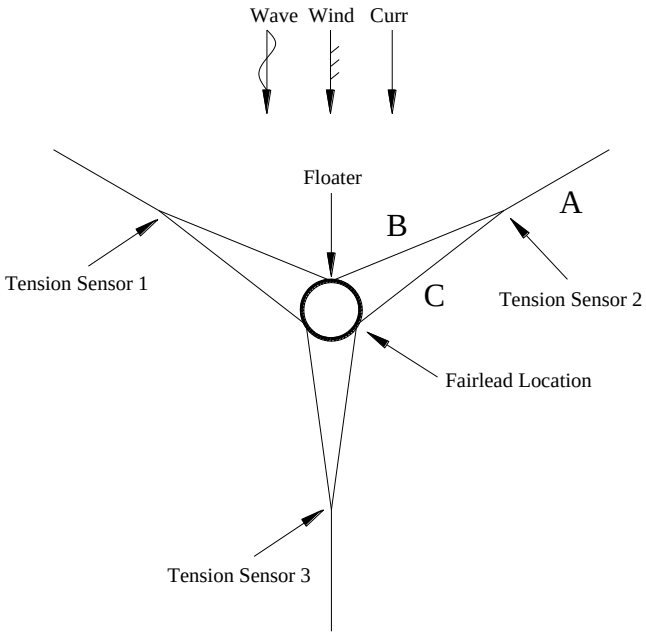

Fig. 3 Mooring system layout

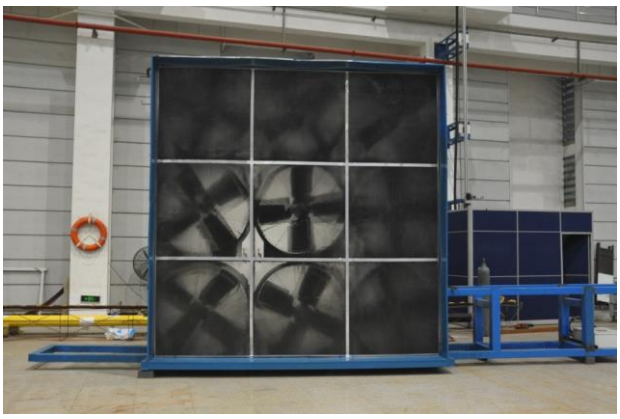

Fig. 4 SJTU Wind Generation System

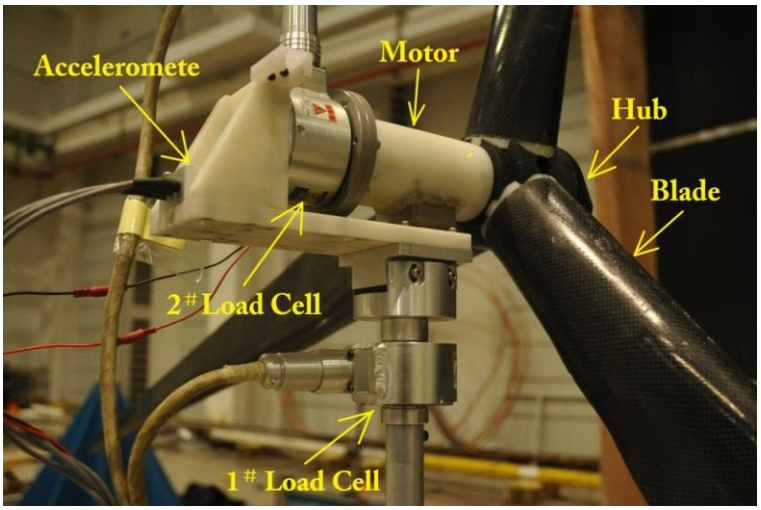

Fig. 5 Assembly configuration of the sensors

Fig. 6 Active optical marker set-up

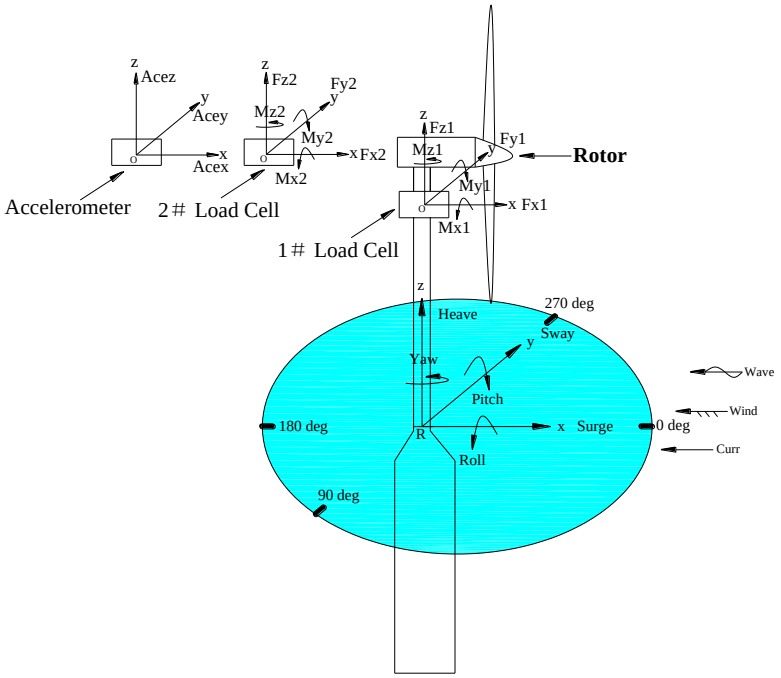

Fig. 7 Definition of coordinates for the 6-DOF motions, forces, moments and accelerations

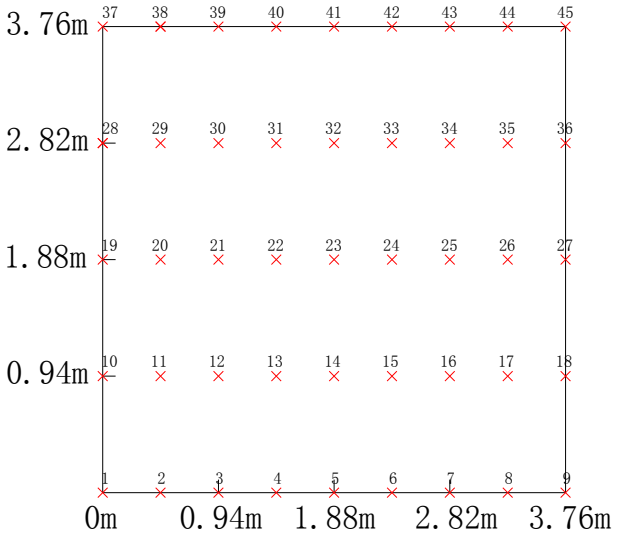

Fig. 8 Location of the wind field measurement points in the array

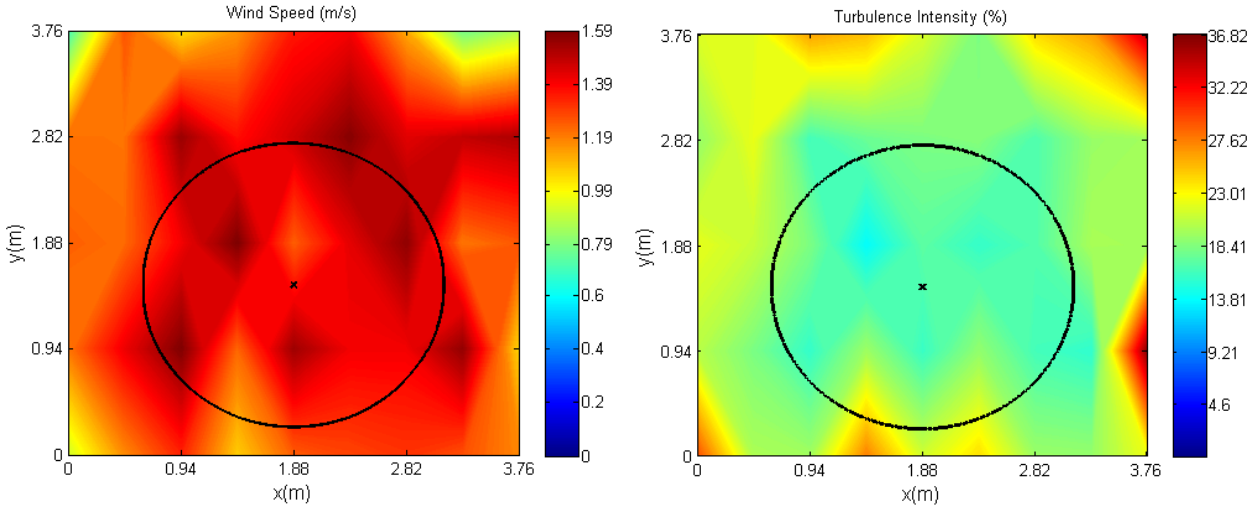

Fig. 9 Wind Speed Profile and Turbulence Intensity at the spar wind turbine model location

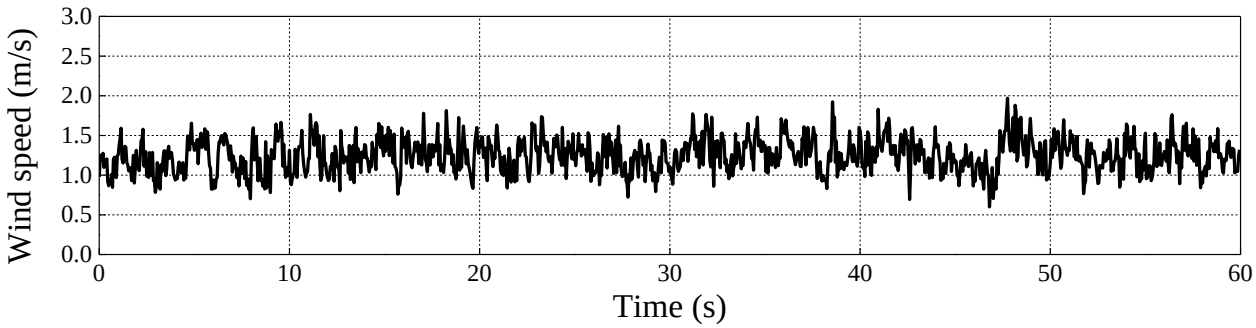

Fig. 10 Sample time history of the wind speed at measurement point number 23

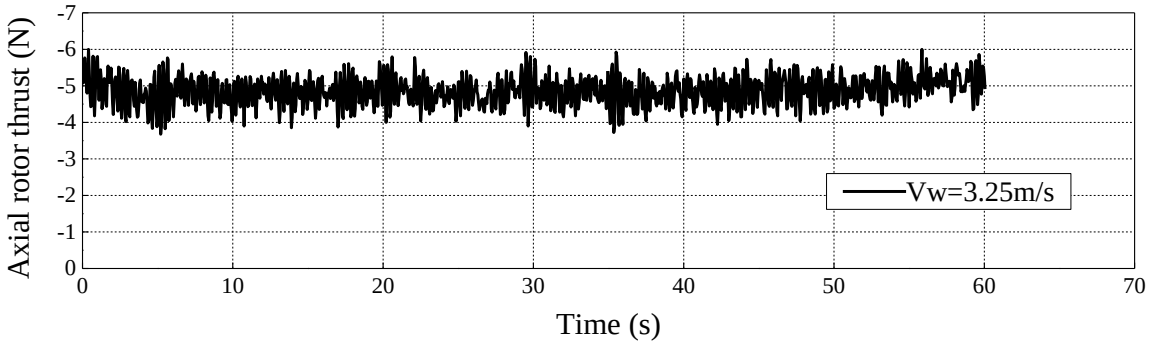

Fig. 11 Time history of the axial rotor thrust for LC6

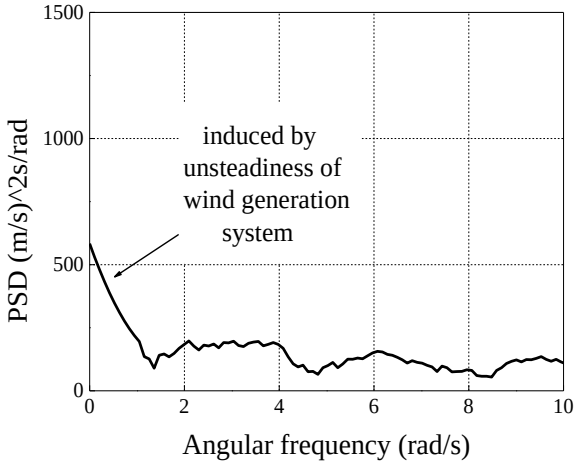

Fig. 12 PSD of the model wind speed at measurement point number 23

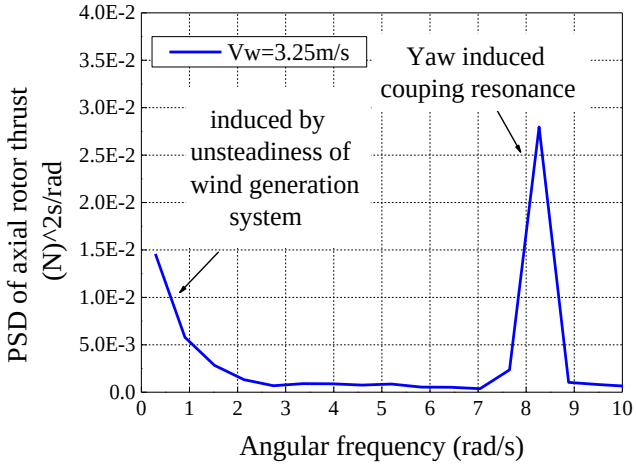

Fig. 13 PSD results of axial rotor thrust for LC6

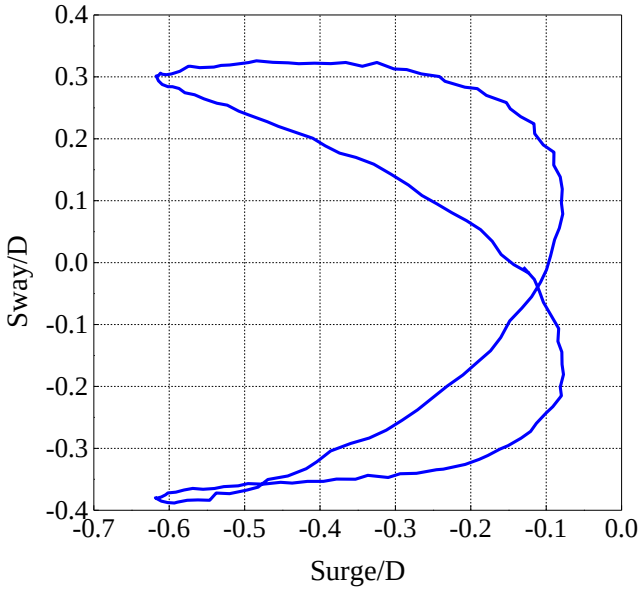

Fig. 14 Trajectory of VIMs in one period with a model current velocity of 0.17 m/s

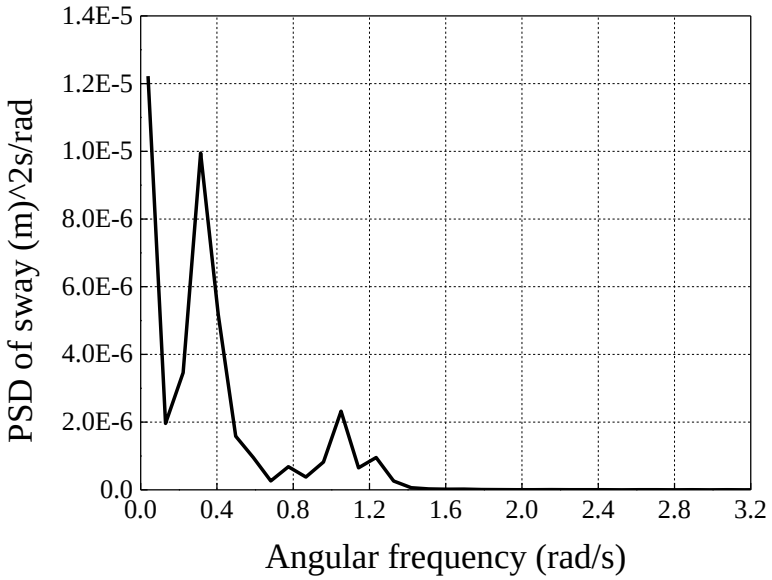

Fig. 15 PSD results of the sway motion based on V_c=0.042 m/s

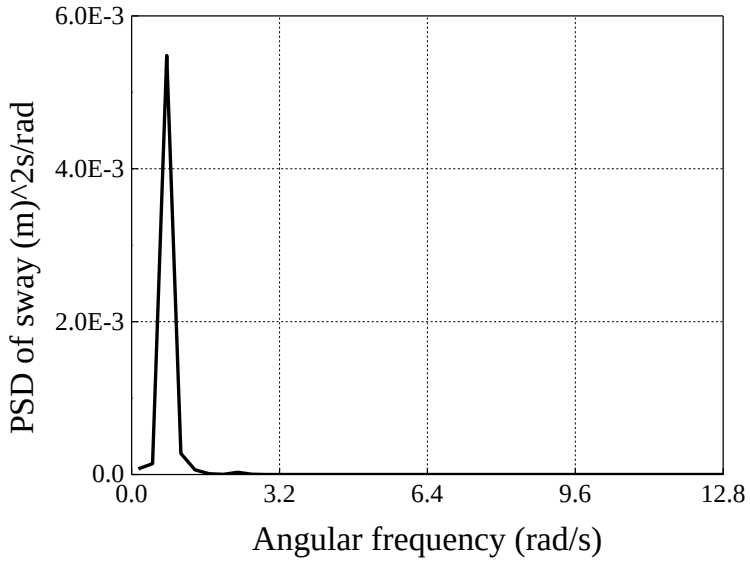

Fig. 16 PSD results of the sway motion based on V_c=0.17 m/s

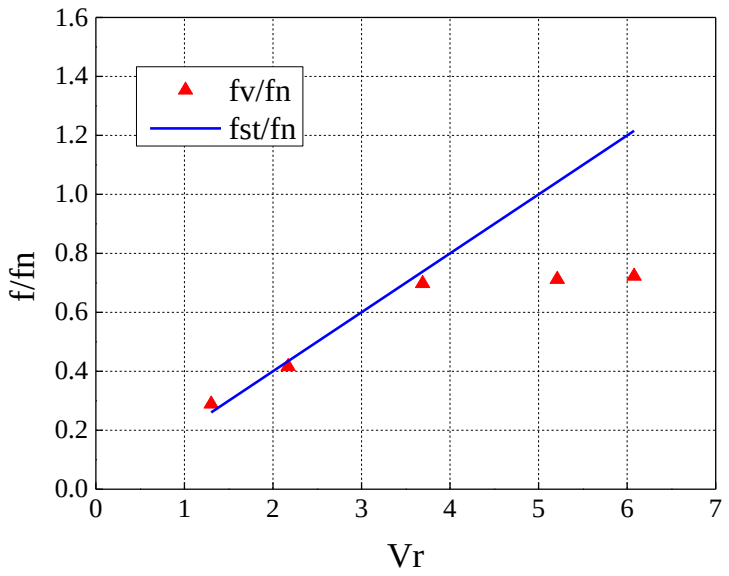

Fig. 17 Frequency ratio of sway as a function of the normalized current velocity

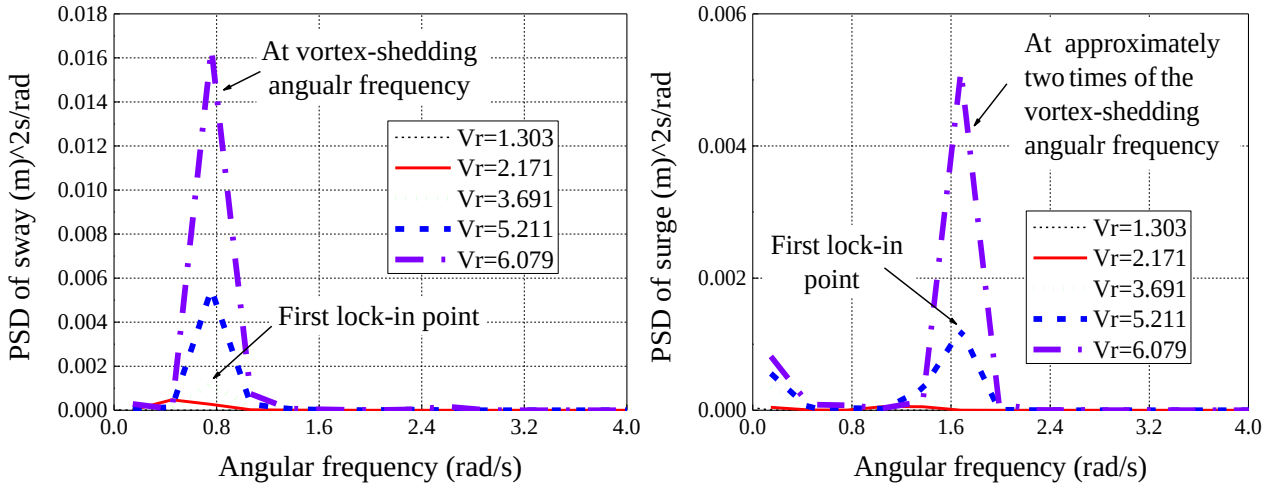

Fig. 18 PSDs of the sway and surge responses for five current velocities

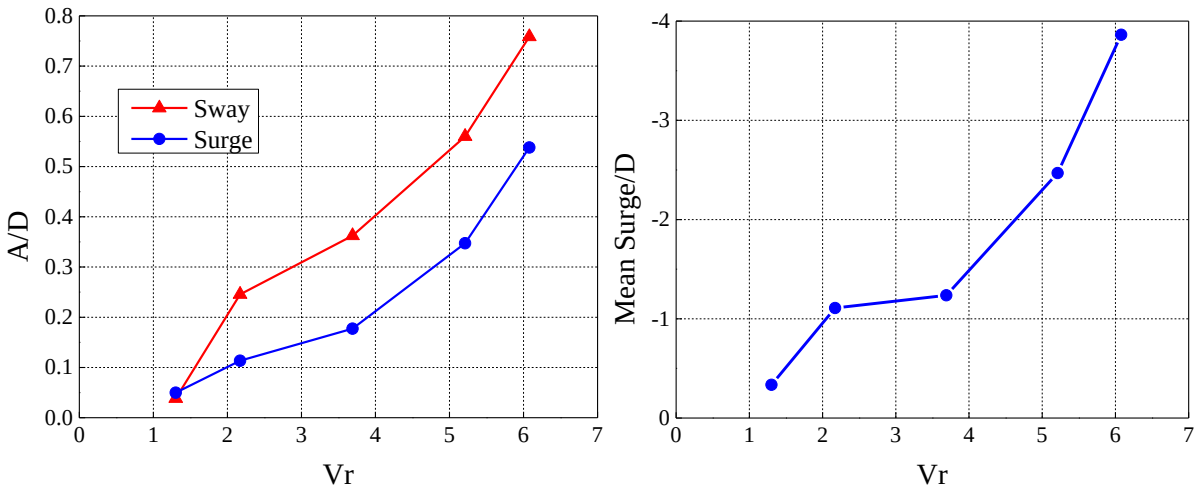

Fig. 19 Normalized amplitude and mean surge as a function of the normalized current velocity

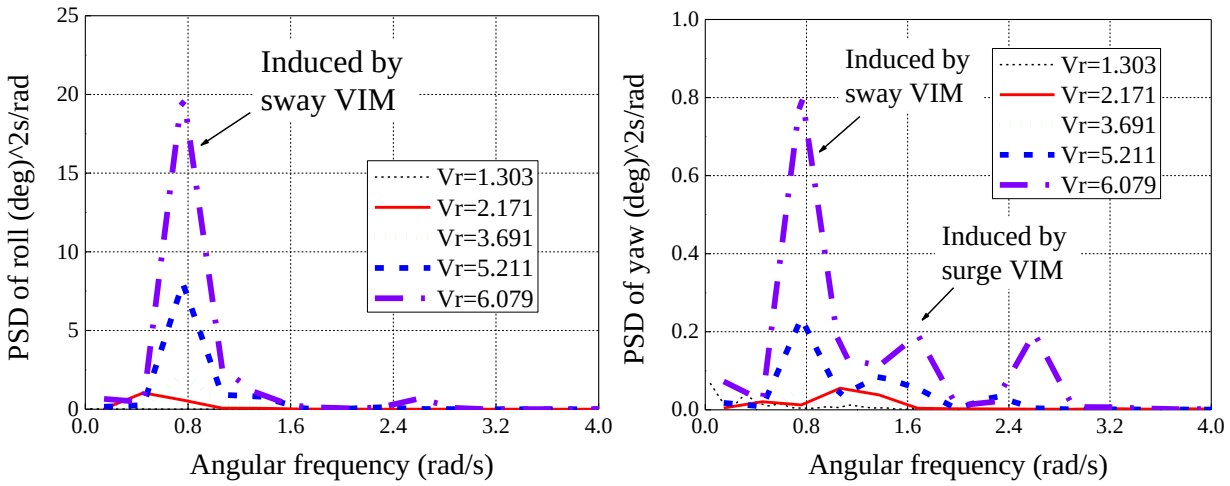

Fig. 20 PSDs of the roll and yaw responses for five current velocities

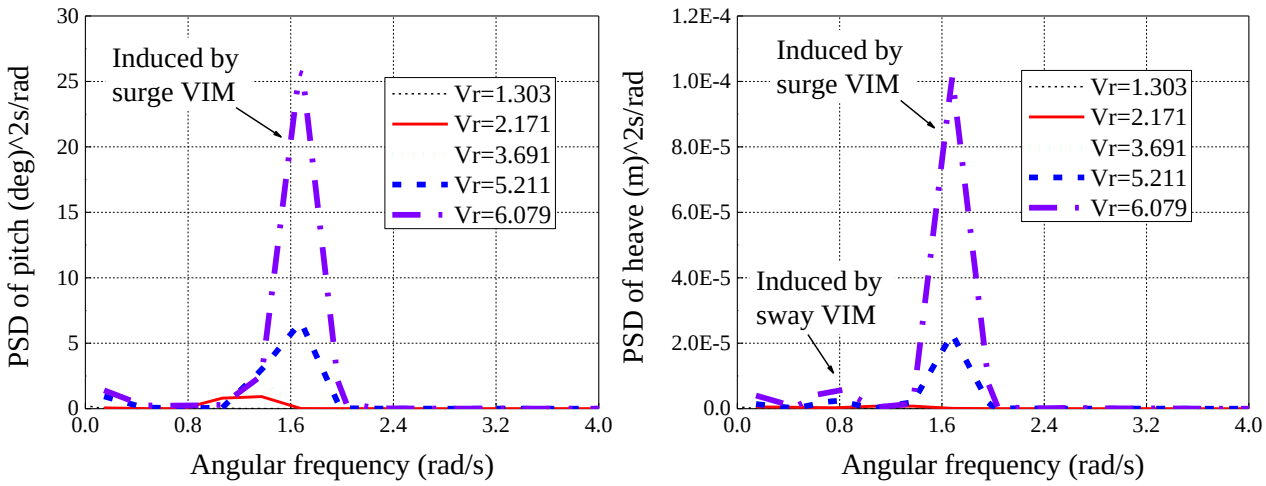

Fig. 21 PSDs of the pitch and heave responses for five current velocities

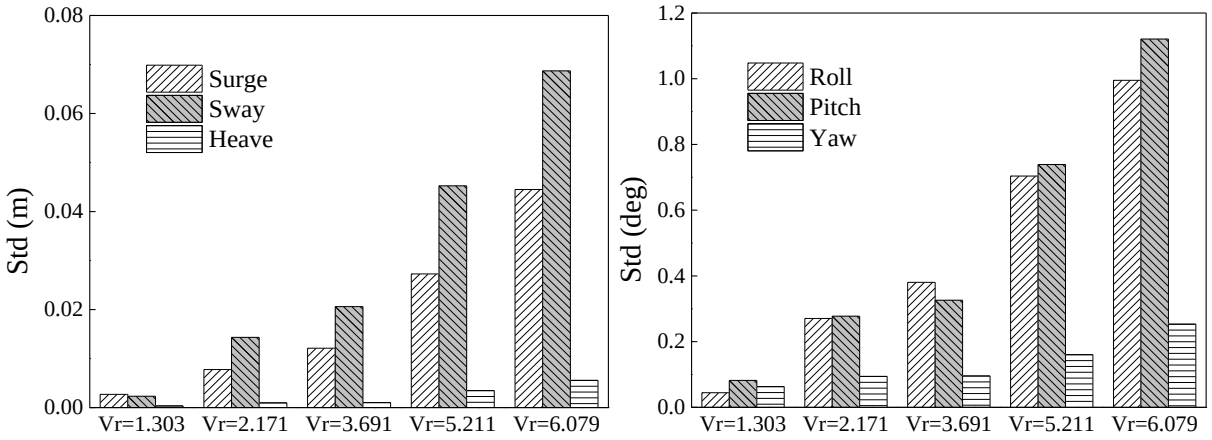

Fig. 22 Comparison of the response standard deviations for translational and rotational motions

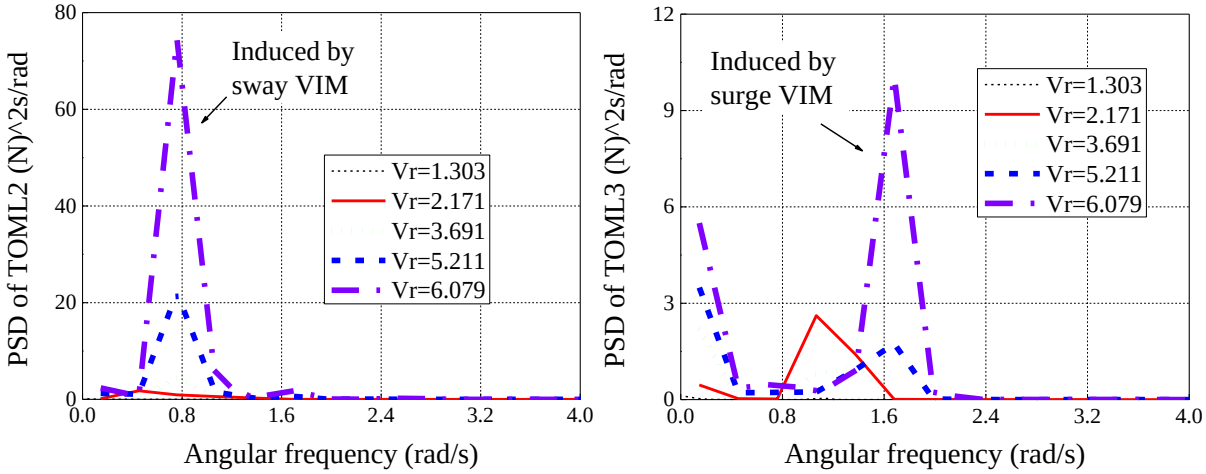

Fig. 23 PSD results of the TOML2 and TOML3 based on various current velocities

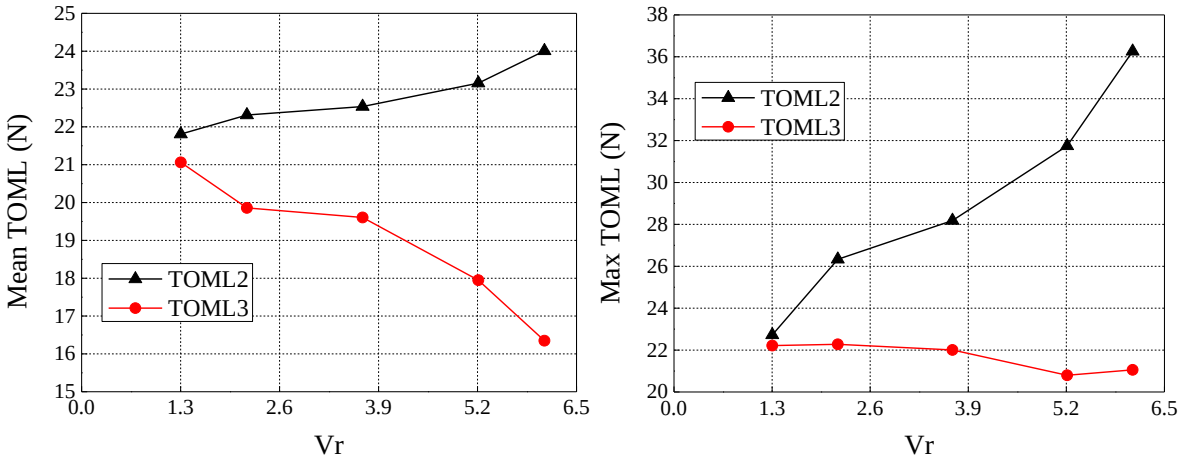

Fig. 24 Mean and maximum TOMLs as a function of the normalized current velocity

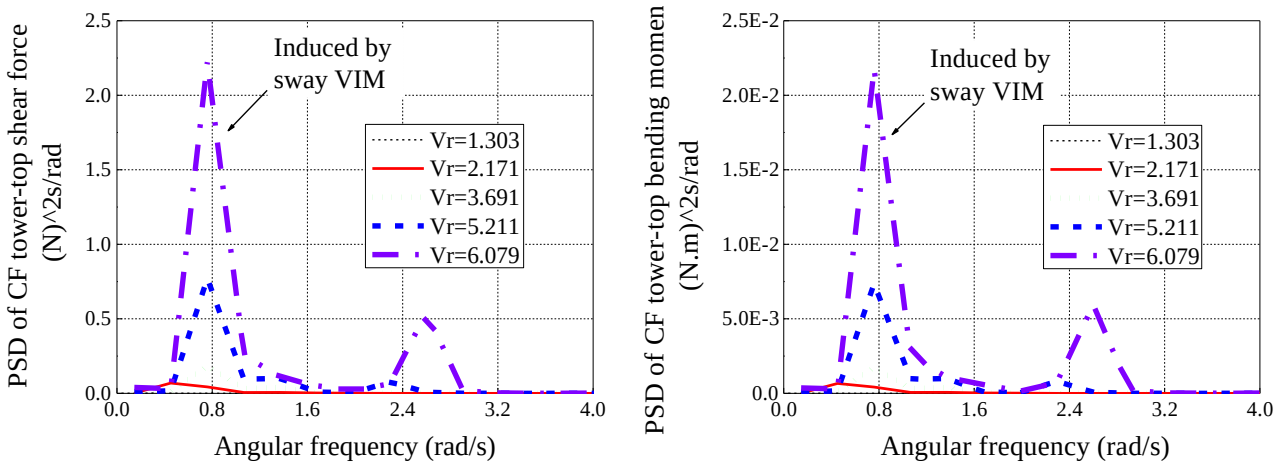

Fig. 25 PSD results of CF tower-top shear force and bending moment based on various current velocities

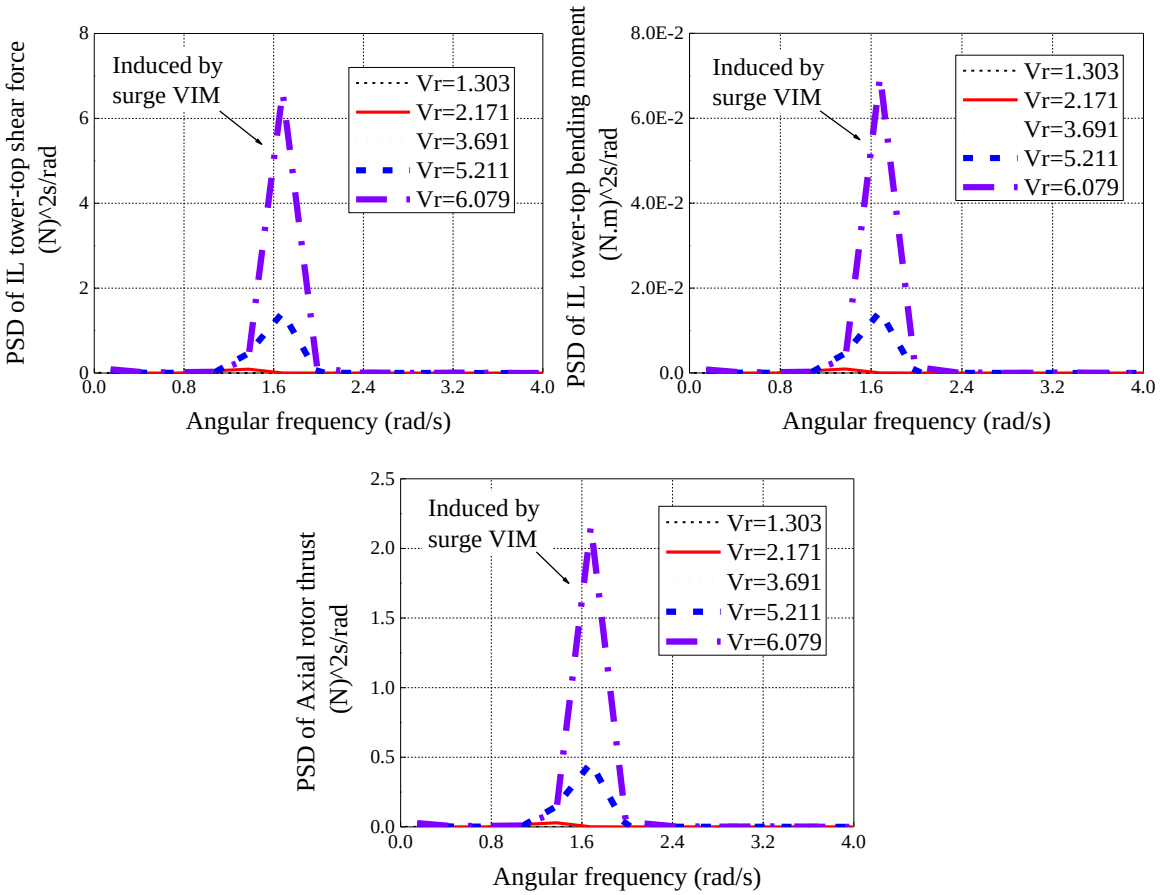

Fig. 26 PSD results of axial rotor thrust, IL tower-top shear force and bending moment based on various current velocities

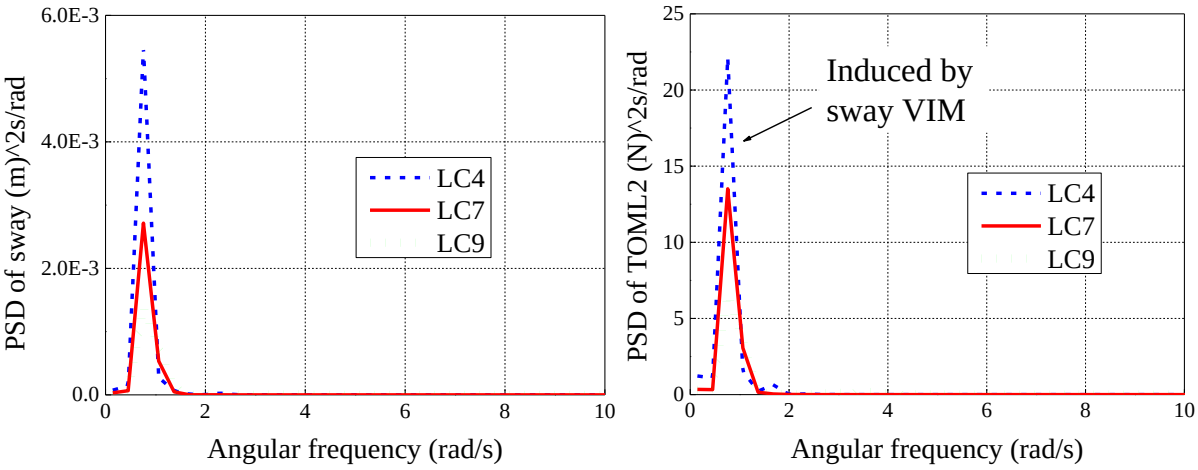

Fig. 27 PSD results of sway and TOML2 for LC4, LC7 and LC9

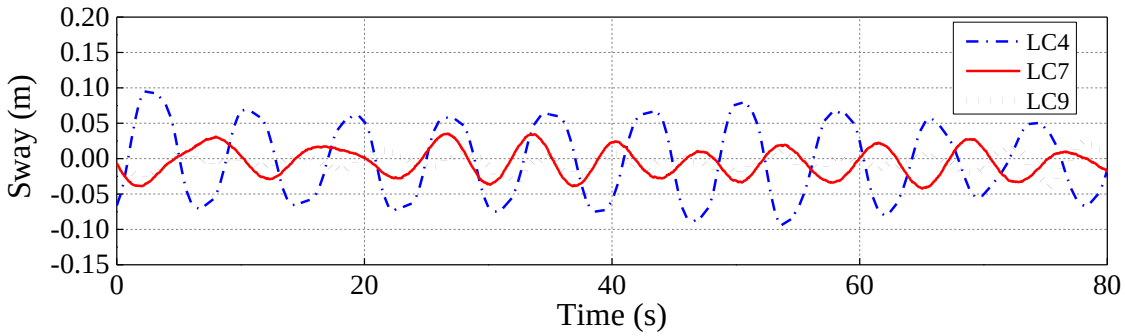

Fig. 28 Time histories of sway based on LC4, LC7 and LC9

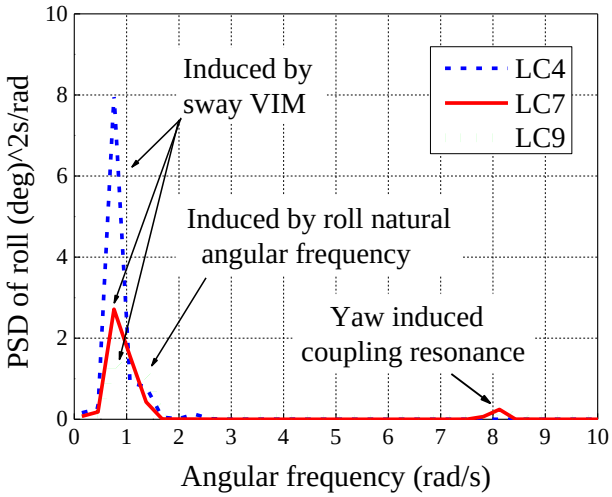

Fig. 29 PSD results of roll for LC4, LC7 and LC9

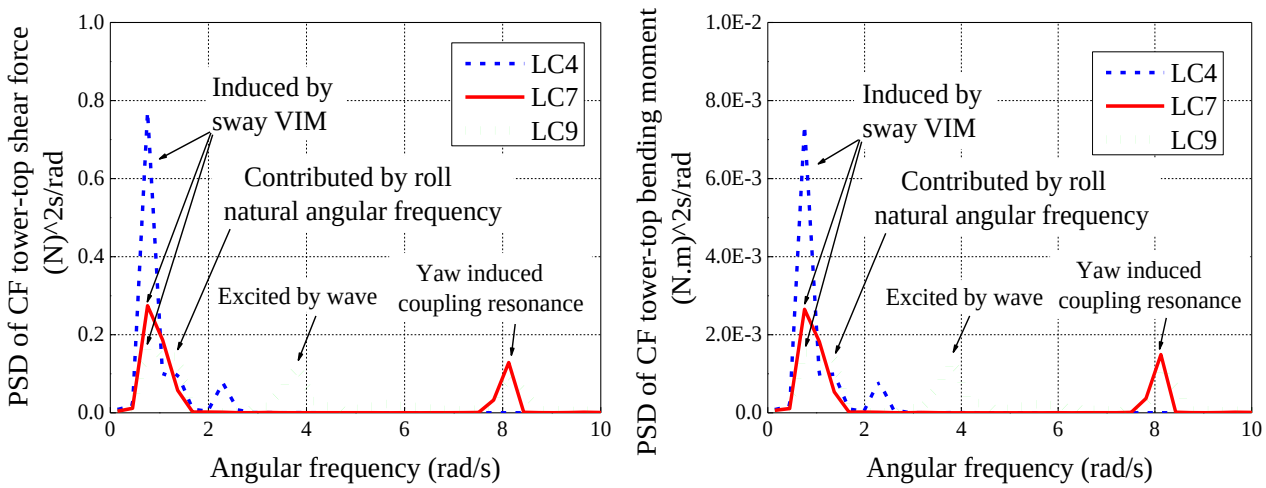

Fig. 30 PSD results of CF tower-top shear and bending moment for LC4, LC7 and LC9

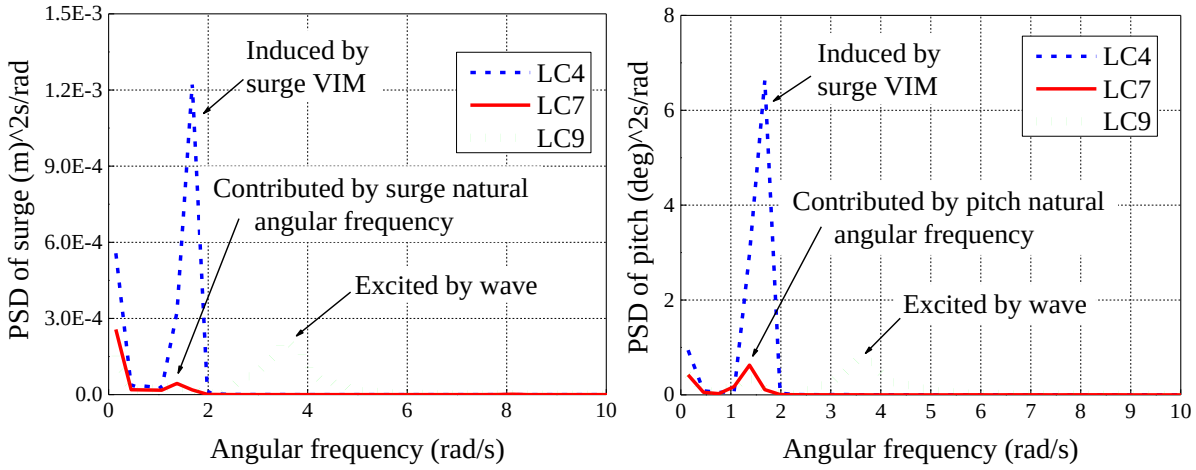

Fig. 31 PSD results of surge and pitch for LC4, LC7 and LC9

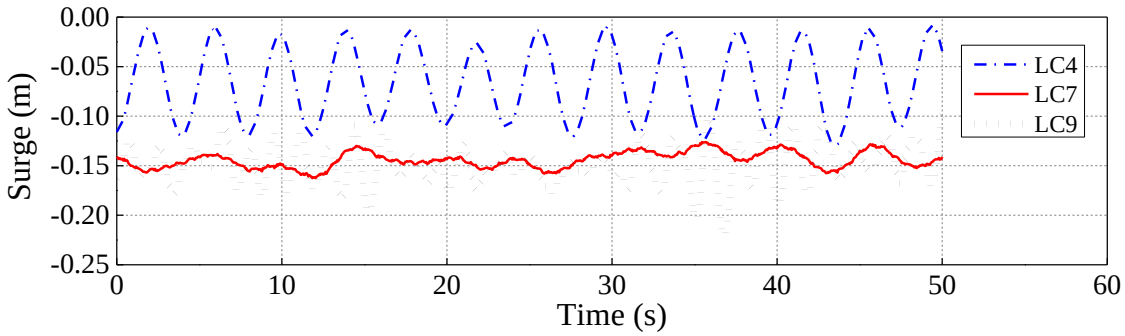

Fig. 32 Time histories of surge based on LC4, LC7 and LC9

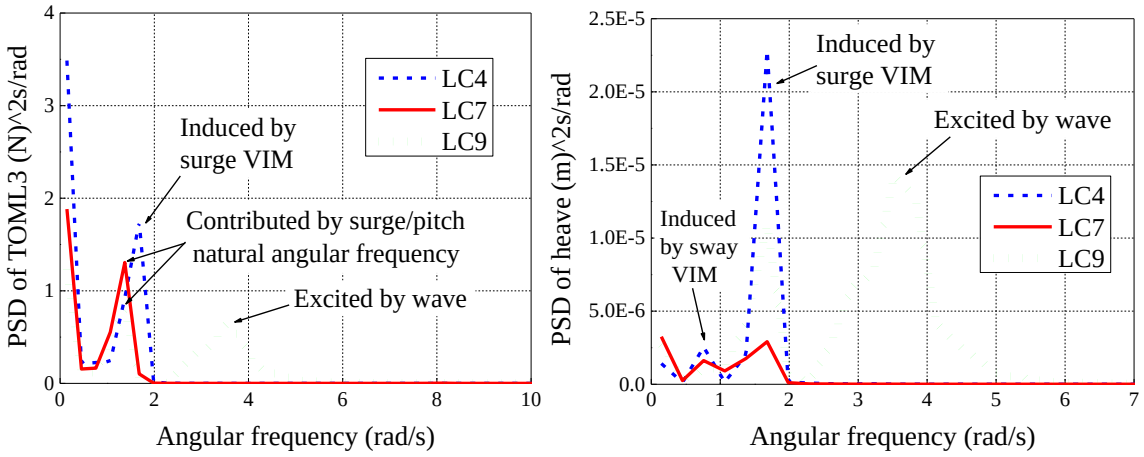

Fig. 33 PSD results of the TOML3 and heave for LC4, LC7 and LC9

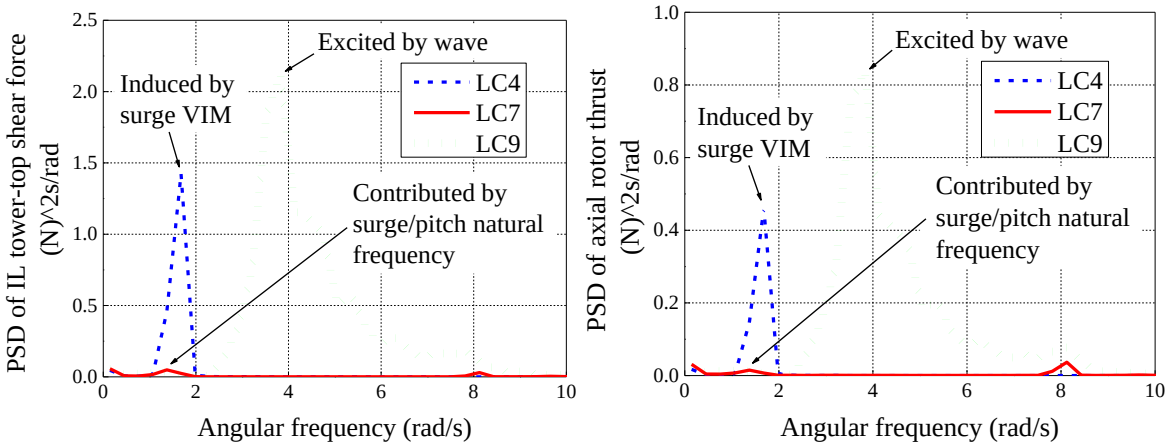

Fig. 34 PSD results of IL tower-top shear force and axial rotor thrust for LC4, LC7 and LC9

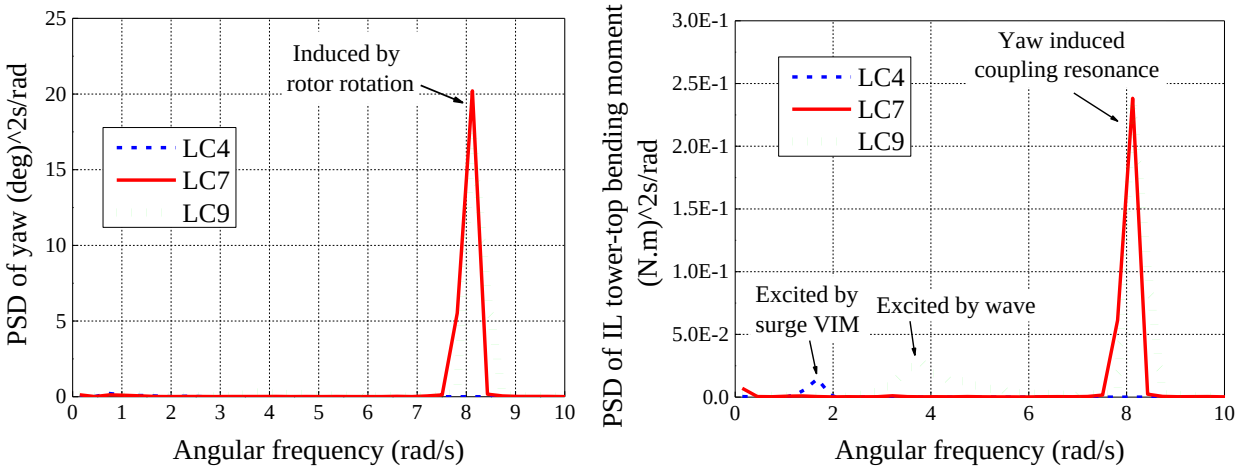

Fig. 35 PSD results of yaw and IL tower-top bending moment for LC4, LC7 and LC9

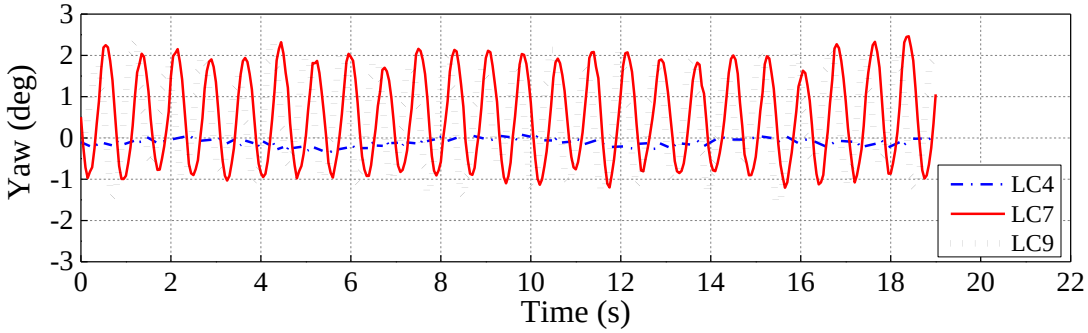

Fig. 36 Time histories of yaw based on LC4, LC7 and LC9

Table 1 Main Properties of the NREL 5 MW reference wind turbine and OC3 Hywind tower

Item	**Unit**	**Designation**
Rated power	MW	5
Rated wind speed	m/s	11.4
Blade length	m	61.5
Blade mass	kg	17,740
Hub diameter	m	3
Hub height	m	90
Hub mass	kg	56,780
Rotor diameter	m	126
Nacelle mass	kg	240,000
Tower mass	kg	249,718
Tower length	M	77.6
CM location of the tower	m	43.4

Table 2 Case definitions of the basin test

Remark	Load case	Full scale					Model scale				
		Current velocity (m/s)	Wind velocity (m/s)	Hs (m)	Tp (sec)	γ	Current velocity (m/s)	Wind velocity (m/s)	Hs (m)	Tp (s)	γ
Current only	LC1	0.3	-	-	-	-	0.042	-	-	-	-
	LC2	0.5	-	-	-	-	0.071	-	-	-	-
	LC3	0.85	-	-	-	-	0.12	-	-	-	-
	LC4	1.2	-	-	-	-	0.17	-	-	-	-
	LC5	1.4	-	-	-	-	0.198	-	-	-	-
Wind only	LC6	-	23	-	-	-	-	3.25	-	-	-
Wind with current	LC7	1.2	23	-	-	-	0.17	3.25	-	-	-
Wind with wave	LC8	-	23	7.1	12.1	2.2	-	3.25	0.14	1.71	2.2
Combination of wind, wave and current	LC9	1.2	23	7.1	12.1	2.2	0.17	3.25	0.14	1.71	2.2

Table 3 Results of the free decay tests

Decay type	Natural period (s)	Natural frequency (Hz)	Natural angular frequency (rad/s)	Damping ratio
Surge	5.724	0.175	1.098	0.038
Sway	5.772	0.173	1.089	0.033
Heave	3.894	0.257	1.613	0.028
Pitch	4.800	0.208	1.309	0.035
Roll	5.033	0.199	1.248	0.031
Yaw	0.841	1.189	7.472	0.086

Table 4 Current velocities and corresponding parameters based on sway

Status	Load case	Current velocity		Reynolds number for model scale	Strouhal number for model scale	Normalized velocity V_r	f_{st}/f_n	f_v/f_n
		full scale	model scale					
Before lock-in	LC1	0.3	0.042	0.752E04	0.2	1.303	0.261	0.289
	LC2	0.5	0.071	1.254E04	0.2	2.171	0.434	0.416
Lock-in	LC3	0.85	0.120	2.132E04	0.2	3.691	0.738	0.698
	LC4	1.2	0.170	3.010E04	0.2	5.211	1.042	0.712
	LC5	1.4	0.198	3.512E04	0.2	6.079	1.216	0.723

Table 5 Statistical results based on LC4 and LC7

Title	Unit	Statistics	Vc=0.17 m/s	Vw=3.25 m/s, Vc=0.17 m/s
Surge	m	Mean	-0.049	-0.143
TOML1	N	Mean	23.348	24.205
		Max	31.044	32.885
TOML2	N	Mean	23.155	23.901
		Max	31.746	31.840
TOML3	N	Mean	17.948	16.597
		Max	20.796	19.265